Charles University
Faculty of Science

Study programme: Modelling of Chemical Properties of Nano- and Biostructures

Mgr. Miroslav Položij

Theoretical investigation of microporous materials for adsorption and catalysis

Teoretické studium mikroporézních materiálů pro využití v adsorpci a katalýze

Doctoral thesis

Supervisor: prof. RNDr. Petr Nachtigall Ph.D.
Consultant: RNDr. Lukáš Grajciar, Ph.D.

Prague, 2017

Prohlášení:

Prohlašuji, že jsem závěrečnou práci zpracoval samostatně a že jsem uvedl všechny použité informační zdroje a literaturu. Tato práce ani její podstatná část nebyla předložena k získání jiného nebo stejného akademického titulu.

V Praze,

Podpis

Acknowledgements

First I would like to express my sincere gratitude to my advisor prof. Petr Nachtigall for the patience and support during all the years I have been his student. His guidance was the first and foremost thing that made the completion of this thesis possible. I also want to thank all my current and former colleagues in our group for the opportunity to work with them and for all their help, which came whenever needed – Miroslav Rubeš, Lukáš Grajciar, Jan Hermann, Ho Viet Thang, Markéta Hezinová, Ángel Morales-García, Junjie He, Pengbo Lyu and Christopher Heard. Many thanks also go to all other people, with whom I have collaborated over the years of my study and who are too many to name here.

I am also deeply thankful to my parents for all the support they gave me and mainly that they led me where I am now and I want to sincerely thank my wife Tina for understanding and her great patience with me.

Miroslav Položij

Abstract: **Theoretical investigation of microporous materials for adsorption and catalysis**

Microporous materials are defined by a presence of pores with diameter smaller than 2 nm. They comprise a large variety of materials from amorphous materials to very well defined crystalline materials like zeolites or metal organic frameworks. Microporous materials are industrially very important group of materials used for adsorption, gas capture, molecular sieving, or heterogeneous catalysis. Zeolites are by far the most important group of microporous materials due to their use as catalysts for the petroleum cracking. One of the main limitations of the zeolite use in catalysis is their limited pore size. This obstacle can be solved by use of hierarchical zeolites with a secondary mesopore network which allows overcoming the diffusion problems.

The aims of this study can be divided into two parts. In the first part, the structures of two-dimensional and hierarchical zeolites were investigated theoretically to identify the structure of new materials and to obtain reliable models to study the hierarchical zeolites. In the second part, the catalytic properties of several microporous materials were modelled to explain their experimental activity.

The results of this thesis were used to identify the structure of a large number of materials, including zeolite SAZ-1, ADOR zeolites IPC-2, IPC-4, IPC-9, or IPC-10, layered zeolites MCM-22P and MCM-56, or metal organic framework CAU-10. In particular, the structure of layered zeolite IPC-1P, derived from zeolite UTL, was investigated together with a large family of zeolites synthetized from it. A large emphasis was given on the correct description of all possible material structures including the structural disorder. The structural disorder was linked to material properties of the layered zeolites with MWW topology and the zeolite SAZ-1. The catalytic activities of metal organic framework CuBTC and Na-grafted zeolite USY were also investigated. Both materials are known experimentally to act as Brønsted bases despite the lack of basic catalytic centres. Their activity was linked to the defect in the structure; either permanent defect on the mesopore surface of USY or dynamically formed defects in CuBTC.

Keywords: Microporous materials, Metal Organic Framework, Zeolite, Density Functional Theory, Modelling, Catalysis, Reaction Mechanisms

Abstrakt: **Teoretické studium mikroporézních materiálů pro využití v adsorpci a katalýze**

Mikroporézní materiály jsou definovány přítomností pórů s průměrem menším než 2 nm. Do této skupiny spadají rozličné materiály, počínaje amorfními materiály a konče dobře definovanými krystalickými materiály, jako jsou zeolity nebo „metal organic frameworks“ (MOF, organokovové krystalické polymery). Mikroporézní materiály jsou velmi významné pro průmysl, kde jsou využívány pro adsorpci, jako molekulová síta nebo jako heterogenní katalyzátory. Nejdůležitější skupinou mikroporézních materiálů jsou zeolity, které jsou využívány jako katalyzátory pro krakování ropy. Využití zeolitů v katalýze je omezeno malým průměrem pórů, které tak nejsou přístupné pro větší molekuly. Toto omezení lze obejít použitím hierarchických zeolitů obsahujících mezopóry, díky kterým mají výrazně lepší difúzní vlastnosti.

Cíle této práce lze rozdělit na dvě části. V první části byla studována struktura vrstevnatých a hierarchických zeolitů s cílem identifikovat strukturu nových materiálů a vytvořit spolehlivé teoretické modely pro studium hierarchických zeolitů. V druhé části práce byly studovány katalytické vlastnosti několika mikroporézních materiálů.

Výsledky této práce byly použity pro identifikaci struktury řady materiálů, včetně zeolitu SAZ-1, zeolitů IPC-2, IPC-4, IPC-9 či IPC-10, získaných metodou ADOR, vrstevnatých zeolitů MCM-22P a MCM-56, či MOF CAU-10. Jedním z hlavních témat práce bylo zjištění struktury vrstevnatého zeolitu IPC-1P, odvozeného od zeolitu UTL, a rozsáhlé skupiny zeolitů, které je možné z IPC-1P syntetizovat. V celé práci byl kladen velký důraz na správný popis možných konformací materiálu a neuspořádanosti struktury, zejména u vrstevnatých zeolitů odvozených od MWW a zeolitu SAZ-1. Mimoto byly studovány katalytické vlastnosti MOF CuBTC a sodné formy zeolitu USY. Oba tyto materiály vykazují aktivitu jako Brønstedovy báze, přestože neobsahují typické bazické skupiny. Aktivita těchto materiálů byla spojena s tvorbou defektů v krystalické struktuře obou materiálů, a to jak trvalých defektů na povrhu mezopórů v USY, tak dočasně tvořených defektů v CuBTC.

Klíčová slova: Mikroporézní materiály, Metal Organic Frameworks, Zeolity, Density Functional Theory, Modelování, Katalýza, Reakční Mechanismy

Contents

List of Figures

List of Tables

List of the Abbreviations

ADOR – Assembly, Disassembly, Organization, Reassembly
CC – Coupled Clusters
CCSD(T) – Coupled Clusters with Singles, Doubles and perturbative Triples
CI – Configuration Interaction
D4R – Double-four membered Ring
DFT – Density Functional Theory
DFT-D – Density Functional Theory with empirical Dispersion
GGA – Generalized Gradient Approximation
HF – Hartree-Fock
IR – Infrared
IZA – International Zeolite Association
LDA – Local Density Approximation
LID – Local Interatomic Distance
MOF – Metal-Organic Framework
MPn – Møller-Plesset perturbation theory to the n^{th} order ($n=2,3\ldots$)
QST – Quadratic Synchronous Transit
PAW – Projector Augmented Wave
pXRD – Powder X-ray Diffraction
S4R – Single-Four membered Ring
SDA – Structure Directing Agent
UC – Unit Cell
vdW-DF – van der Waals Density Functional
WF – Wave Function

1. Introduction

Microporous materials are one of the industrially most important types of materials thanks to their widespread use as sorbents, ion-exchangers, and catalysts. Zeolites are by far the most important microporous materials due to their use as catalysts for the crude oil processing and in petrochemistry. Zeolites are crystalline aluminosilicates containing pores and cavities with size up to 1.5 nm. The zeolite internal surface contains large concentration of extra-framework cations like Na^+, Li^+, Ca^{2+}, or H^+ that act as very strong active sites with Lewis or Brønsted acid character. Nevertheless, the size of micropores does not allow larger molecules to reach the active sites, which rather limits the zeolite use. This obstacle can be solved by using hierarchical zeolites, which combine the standard zeolite microporosity with mesoporosity, and thus have superior diffusion properties. An interesting group of hierarchic zeolites are two-dimensional zeolites, which are formed by very thin layers of zeolites and thus have a huge external surface accessible for adsorption. However, structure of hierarchical zeolite often exhibits a large degree of disorder, which makes them very hard to characterize.

Metal organic frameworks (MOFs) are another interesting group of microporous materials. They consist of the inorganic nodes (metal ions or small metal oxide clusters) interconnected by organic linkers. MOFs are now widely studied as very promising sorbents and catalysts. Their internal surface area surpasses that of zeolites and they can contain a large variety of active sites ranging from strong Lewis acid or redox centres represented by metal ions to both acidic and basic sites on organic linkers. Furthermore, structure and properties of metal organic frameworks can be easily designed and tuned by the choice of the building blocks, which allows tailoring of the materials for specific applications.

Investigation of mechanisms of catalytic processes inside microporous materials is a challenging task for experimental methods, because the active sites are hidden inside micropores and their structure is often not exactly known. Computational chemistry can study these materials on an atomic level, which allows to probe the structure of active materials and individual active sites, study their sorption properties, and also to directly model the mechanism or chemical reactions.

The aims of this study are twofold: First, structures of two-dimensional and hierarchical zeolites were investigated theoretically to identify the real structure of experimentally known materials and to obtain reliable models to study the hierarchical zeolites. Second, the catalytic properties of several microporous materials were modelled to explain their, often unexpected, experimental activity.

Following systems were investigated:

1) Structure of zeolites
   i. Structure of two-dimensional zeolite IPC-1P and structures of new zeolites that can be obtained from IPC-1P.
   ii. Structure of zeolite SAZ-1 and two-dimensional zeolite SAZ-1P and structures of new zeolites that can be obtained from SAZ-1P
   iii. Structures of two- and three-dimensional zeolites with MWW topology
   iv. Structure of hierarchical zeolite USY grafted with Na^+ ions.

2) Catalytic properties of microporous materials
   i. Na^+ grafted hierarchical zeolite USY activity in basically catalysed aldol condensation reaction.
   ii. Photoreactivity of NO_2 functionalized metal organic framework CAU-10, which spontaneously generates long-lived radicals after irradiation.
   iii. Catalytic activity of metal organic framework CuBTC in the Knoevenagel condensation reaction.

The work was done in a close collaboration with experimental groups in Czech Republic and abroad. The collaboration between the theory and the experiment is necessary for ensuring the relevance of the studied phenomena to real systems. Research was supported by several projects of the scientific group of Prof. Petr Nachtigall; Czech Science Foundation project (Centre of Excellence) “Intelligent Design of Nanoporous Adsorbents and Catalysts” and European Union 7th Framework Programme project CASCATBEL (CAScade deoxygenation process using tailored nanoCATalyst for production of BiofuELs from lignocellulosic biomass”). Also, a large part the work reported in the thesis was done as a part of my GAUK project entitled “Theoretical investigation of structure and catalytic activity of hierarchical zeolites”. The work reported in this thesis was reported so far in eight publications in international scientific journals, including Nature Chemistry, Chemistry of Materials or Dalton Transactions.

The thesis is organized as follows; Chapter 2 covers a brief background on the standard and hierarchical zeolites and metal organic frameworks. Chapter 3 introduces the computational methods and models used through the study, together with a brief introduction into the DFT methods. The main results and discussion are reported in Chapter 4, which is divided into two thematic blocks; i) investigation of the zeolite structure (Chapter 4.1) and ii) investigation of the catalytic applications of microporous materials (Chapter 4.2). The Chapter 4.1 covers the investigation of structures of the zeolites derived from layered IPC-1P, SAZ-1P, and MCM-22P zeolites and also the structure of hierarchical USY zeolite. The Chapter 4.2 covers the investigation of the catalytic properties of Na-grafted hierarchical USY zeolite, the catalytic properties of metal organic framework CuBTC, and photoreactivity of the CAU-10-NO_2. The Chapter 5 finally summarizes the results and general trends observed in the project.

2. General Background

Microporous materials are defined by a presence of pores with diameter smaller than 2 nm.[1] They comprise a large variety of materials from amorphous materials, *e.g.*, microporous polymers and active carbon, to very well defined crystalline materials, *e.g.*, zeolites or metal organic frameworks. Microporous materials are industrially very important group of materials used for adsorption, gas capture, molecular sieving, ion exchange or heterogeneous catalysis. Their applicability in the industrially important processes is motivated by their large inner surface (10^2-10^3 m^2 g^{-1}), structural properties (topology of microporous network) and presence of catalytically active sites. This thesis focuses on the investigation of structure and properties of zeolites, metal organic frameworks, and of hierarchical microporous-mesoporous materials (mesopores are defined by diameter of 2-50 nm) derived from zeolites.

2.1 Zeolites

Zeolites[2] are crystalline aluminosilicates containing pores or cavities with diameter up to 1 nm. The zeolite micropores can be formed as simple 1D channels or 2D/3D networks of intersecting channels and cavities. The size of pores is defined by the number of T-atoms enclosing the cut through the channel and varies from 8T to 18T rings. They consist primarily of the SiO_4 tetrahedra linked by shared oxygen atoms. The silicon can be substituted by other elements; mainly Al, but also by other atoms, *e.g.* Ge, Fe, B, etc. However, the substitution of trivalent elements into the tetrahedral crystallographic position introduces a negative charge on the framework. The charge is compensated by extra-framework cations, typically by Na^+, Li^+, Ca^{2+}, or H^+. The ions are often present in a large concentration on the zeolite internal surface and they often have a very strong catalytic activity. The extra-framework cations are the source of the zeolite most important applications, namely in catalysis and as ion-exchangers.[2]

Zeolites are prepared by hydrothermal-solvothermal synthesis. The synthesis requires a source of silica and alumina (or other ions), aqueous solution of strong bases (mainly alkali metal hydroxides), and often also structure directing agents (SDA), which are organic molecules that template the zeolite synthesis. The synthesis proceeds under high temperatures and pressures in autoclave for several hours or rather days. The formation of a particular zeolite depends on the set of reaction conditions including pH, reactants ratios, nature of SDA, and also time. The mechanism of the solvothermal synthesis is not known and the zeolite produced from each set of reaction conditions thus cannot be predicted.[3, 4]

There are more than 230 known zeolite frameworks approved by International Zeolite Association (IZA, this number also includes aluminophosphates with zeolitic structure).[5] The zeolite frameworks are denoted by three letter codes assigned by IZA, but individual zeolites are commonly identified also by the original name granted after the synthesis, which most often consists of a three-letter code and a number (each laboratory customarily uses the same code for all materials synthetized therein). There are often more zeolites assigned to one framework type; *e.g.* zeolites MCM-22 and MCM-47 both have MWW structure, but differ in synthetic procedure.

The number of experimentally known zeolites is very low compared to the number of theoretically predicted “hypothetical zeolites”.[6] Several feasibility criteria have been put forward to explain the inabil1ity to access the majority of possible framework structures. One of such criteria is so called feasibility factor ϑ, which measures how far lies the zeolite from the energy-density correlation of the experimentally known zeolites (Figure 2.1).[7, 8] All experimentally known zeolites lie very close to the correlation line, which suggests that the solvothermal synthesis can access only a very small window of possible zeolite frameworks. Another criterion is a set of so-called Local Interatomic Distance criteria (LID), which assumes that zeolites have to obey a set of rules on the interatomic distances and angles.[9] The LID criteria state that the tetrahedra in zeolites have to be close to the ideal tetrahedron structure in terms of distances and angles and that the Si-O, Si-Si and O-O distances in zeolites should be uniform and belong to only a narrow interval of possible values fitted from the existing zeolites. All known zeolites obey the LID criteria.

The main field of application of zeolites is the industrial catalysis.[2, 10] The extra-framework cations in zeolites are very strong acidic catalytic sites, either Lewis in case of metal cations or Brønsted in case of protons. The most important catalytic process

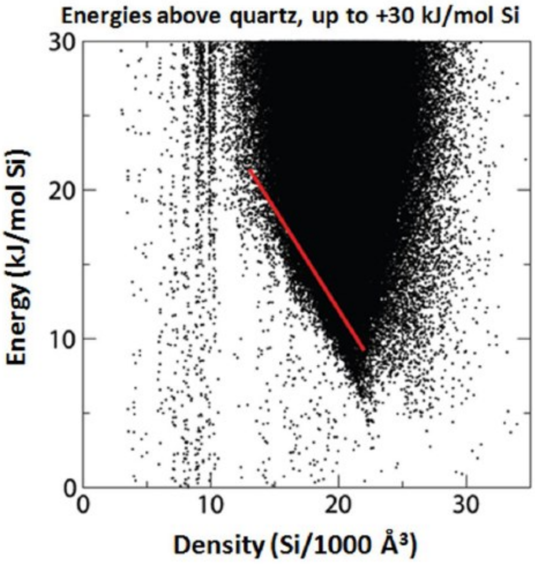

Figure 2.1 – Plot of calculated framework energies vs. framework densities of hypothetical zeolites. The red line is a liner regression of values for experimentally known zeolites. Reproduced from Ref [8] with permission of the PCCP Owner Societies.

using zeolites is the crude oil cracking. Only about 17 of more than 200 zeolites are commercially used; it is mainly zeolite FAU, which makes most of the FCC (Fast Catalytic Cracking) catalysts, but also zeolites MFI, MWW or CHA are used. Most of the zeolite catalysis uses their acidic properties, but they can be also used as redox catalysts[10] (mainly after incorporation of heteroatoms like Ti into the framework) or as basic catalysts.[11] Basicity in zeolites is traditionally obtained through the heavy alkali metal extra-framework cations, Cs^+ in particular. Basic zeolites can also be obtained by various post-synthetic approaches like alkali metal cluster impregnation, or grafting of basic organic molecules.

2.2 Hierarchical zeolites

One of the main limitations for the zeolite use in catalysis is their limited pore size, which prevents adsorption of larger reactants inside the micropores. This obstacle can be overcome by the use of hierarchical zeolites containing a secondary macro- or mesoporous network which allows overcoming the diffusion problems. The catalytic properties of hierarchical zeolites are inherited from the original zeolite or can be introduced by various post-synthetic treatments.[12] Hierarchical zeolites can be prepared by various methods, including zeolite synthesis on a mesopore-sized template diameter, synthesis of two-dimensional materials with large external surface,[13, 14] synthesis of nano-sized zeolite crystals with inter-crystal mesopores,[15] or by different post-synthetic methods like demetallation.[16] The demetallation (desilication or dealumination) is probably the most common method to introduce the mesopores into zeolites, which is achieved by treatment by mineral acids or bases (depending on the leached metal). Thus created mesopores have undefined structure of mesopore surface. Also, the treatment of the zeolite by acids and bases is often accompanied by destruction of the significant portion of active sites. Nevertheless, the improved diffusion properties often lead to an overall increase of the zeolite activity.[12]

Some zeolites can be synthetized in a form of thin layers, often only one unit cell (UC) wide.[14] These materials thus have a huge external surface that is accessible to bulkier molecules. Most of these layered (two-dimensional) zeolites are obtained during the standard 3D zeolite synthesis as a layered precursor. Some of the 2D zeolites are in principle not zeolites due to presence of large amount of T-atoms that are not connected to four framework atoms (the surface is terminated with silanols) and due to the lack of micropores that are only formed in the 3D zeolite in-between the original layers. The most important 2D zeolite is MCM-22P with MWW topology, which was the first discovered layered zeolite.[17] It is formed as a primary product of the MCM-22 zeolite synthesis, whereas the MCM-22 is obtained by calcination of MCM-22P layers. The MCM-22P layers can undergo various post-synthetic modifications,[14] including “interlayer expansion” by additional silicon atoms, forming O-Si-O linkers in-between the layers, which enhances the porosity.[18] Other important modification is swelling by large organic molecules and subsequent pillaring by amorphous silica, which introduces mesopores in the structure (MCM-36 material).[17] A large set of other materials can be also formed, *e.g.*, delaminated layers in material ITQ-2,[19] disordered layered zeolite MCM-56[20] or even hybrid organic-inorganic materials (Figure 2.2).[21]

About 15 zeolites are known presently in the layered form, similarly to the case of MWW described above.[14] Nevertheless, some layered precursors can belong to more than one 3D zeolites, particularly the FER and CDO zeolite having the identical ferrierite (*fer*) layers, and similarly for zeolites CAS and NSI. The *fer* layers in FER zeolites are related by mirror plane, whereas in CDO zeolite they are products of direct

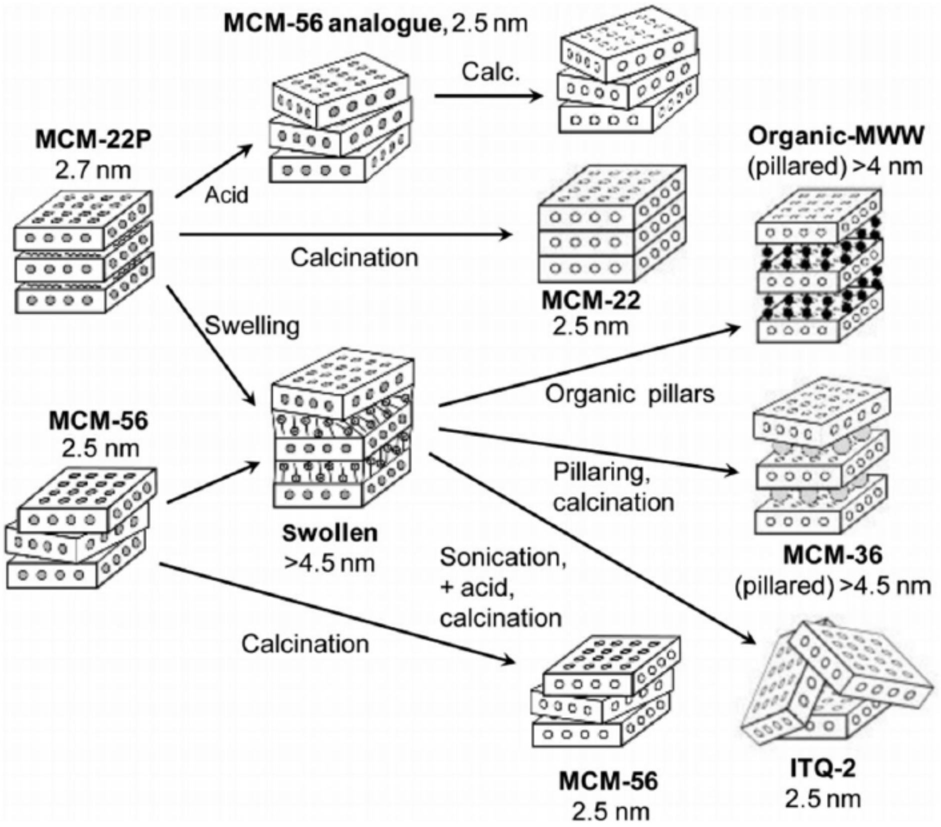

Figure 2.2 – The family of materials derived from the 2D zeolites with MWW framework. Reprinted with permission from [22]. Copyright 2015 American Chemical Society.

translation along layer normal. The FER zeolite thus has structure with 10-6 rings and CDO 8-8 rings. This suggests that even other zeolite layers can have more possible arrangements producing different 3D materials.

2.3 Metal Organic Frameworks

Metal organic frameworks (MOFs) are microporous materials containing metal ions or inorganic clusters connected via organic linkers to well organized 3D frameworks.[23] There is a large variability in MOF structures coming from the number of possible metals used and mainly from the large variability of organic linkers. In principle, any poly-substituted organic molecules with a rigid structure (mostly substituted conjugated aromatic systems) can be used as linkers in MOFs. MOF crystal structures exhibit a large porosity, often exceeding other microporous materials like zeolites; the internal surface can reach even 6000 m^2 g^{-1}. MOFs are generally less stable than zeolites due to lower thermal stability of organic linkers and also susceptibility to hydrolysis of the coordination bonds between metal and organic linkers.

Metal organic frameworks can contain a large variety of catalytically active sites originating both from inorganic and organic parts of the framework.[24] Their activity is directly inherited from the individual constituents; thus, MOFs represent a heterogeneous microporous alternative to the commonly used homogeneous catalysts. The most studied MOF catalysts contain open metal sites that can serve as a Lewis acidic or redox catalysts, *e.g.*, HKUST-1[25] (also called CuBTC) or MIL-100 and MIL-101.[26, 27] These MOFs are among the cheaper and more stable MOFs. Furthermore, MOFs may have also the Brønsted base or Brønsted acid sites, which originate typically from the organic linkers or molecules grafted to the internal surface.[28, 29] Catalytic activity of MOFs can also benefit from the fact that active sites are present in high concentration and, thus, it is possible for several catalytic centres to participate in the reaction simultaneously.[30] Lastly, the lower MOF chemical stability often results in the large concentration of structural defects that can also serve as important catalytic sites.[31] Despite all listed catalytic properties of MOFs they still have not found any industrial application due to their low stability; however, their potential use especially in the fine chemical synthesis makes them very appealing topic of study.[32]

3. Methods and Models

3.1 Methods

3.1.1 DFT

Quantum chemical methods can be divided into two main groups; methods based on the wave function Ψ (WF) and methods based on the electron density.[33] The first group represents the system by a 4N-dimensonal function (N is number of electrons) describing the properties of all electrons in the system. The original, but very approximative, method used to solve the WF is Hartree-Fock (HF). The system representation can be systematically improved by using post-HF methods, mainly Møller-Plesset perturbation theory up to the nth order (MPn), configuration interaction (CI), and coupled cluster methods (CC). However, the computational cost of the post-HF methods rises tremendously with the number of electrons. The computer time in the "golden-standard" method, CCSD(T) (couple-cluster method considering single and double excitations explicitly and accounting for the effect of triple excitations at the perturbation theory level) scales with N^7. The most precise methods therefore cannot be used for large systems.

An alternative approach to represent the system uses the electron density ρ, which depends only on three spatial variables (for each spin).[34] The electron density directly depends on the WF;

$$\rho(\mathrm{r}) = N \int \dots \int \Psi^*(\mathrm{x}, \mathrm{x}_2 \dots \mathrm{x}_N)\Psi(\mathrm{x}, \mathrm{x}_2 \dots \mathrm{x}_N)\, d\mathrm{x}_2 \dots d\mathrm{x}_N. \qquad (1)$$

The density functional theory (DFT) methods are based on the expression of the system energy as a functional of the electron density;

$$E[\rho(\mathrm{r})] = T_{ni}[\rho(\mathrm{r})] + V_{ne}[\rho(\mathrm{r})] + V_{ee}[\rho(\mathrm{r})] + \Delta T[\rho(\mathrm{r})] + \Delta V_{ee}[\rho(\mathrm{r})], \qquad (2)$$

where T_{ni}, V_{ne} and V_{ee} are the kinetic energy, electron-nucleus interaction energy and electron-electron interaction energy within the reference model of non-interacting electrons; ΔT_{ni} is a correction to the kinetic energy coming from the electron-electron interactions, and ΔV_{ee} comprises corrections to electron-electron interactions coming from the electron self-interaction, electron exchange, and electron correlation. The last two terms are commonly merged into the exchange-correlation functional $E_{XC}[\rho(\mathrm{r})]$ (E_{XC} is often divided into separate exchange and correlation functionals). The first three terms in Equation 2 can be solved exactly; however, a form of the exchange-correlation functional is not known and the accuracy of the method is always dependent on the selection of the particular functional.

Unlike the post-HF method series, the DFT does not allow for the systematic improvement of the accuracy. However, there are several types of DFT methods that differ in the approach to the E_{XC} functional and ultimately also in the accuracy. One of the simplest methods is the LDA (Local Density Approximation) method, which is only dependent on the local electron density and the LDA E_{XC} is based on the homogeneous electron gas. LDA is commonly used in solid state physic for prediction of electronic properties of materials but it is not suitable for use in chemistry. A significant improvement is achieved by making E_{XC} functional dependent on both local value of density and its local gradient, resulting in Generalized Gradient Approximation (GGA) functionals.

There is a large variety of GGA functionals. They often are fitted to the experimental data to achieve better accuracy for the specific field of use. The most commonly used GGA functionals with empirical parameters are BLYP (Becke's exchange functional[35] and Lee-Yang-Par correlation functional[36]) or PW86 (Perdew 86 correlation functional)[37], whereas the most common functionals with no empirical parameter are PBE (Perdew-Burke-Ernzerhof, both exchange and correlation parts)[38] or PW91 (Perdew 91 correlation functional).[39] The accuracy of GGA functionals approaches the MP2 level at lower computational cost, which makes them a popular choice in chemistry, especially for large systems studied in the material chemistry. Nevertheless, the accuracy of the DFT functionals can be further improved. One of the possible ways to go are the *meta*-GGA functionals that depend on the first and second derivatives of the electron density. However, the improvements are not significant compared to the increased computational cost. The other options are hybrid DFT functionals, which partially incorporate the HF exchange into E_{XC} functional. The cost of hybrid DFT functionals is higher than that of pure GGA functionals, which makes them less viable for large systems (hundreds of atoms). However, they are the most popular choice for the description of smaller molecules and their chemical properties, including chemical reactivity. The most common hybrid functionals are B3LYP (three-parameter functional derived from BLYP)[35] and Minnesota functionals form, particularly M06.[40] Both these functionals have comparable accuracy with the MP2 method and are often superior to it in the description of molecular geometry. The GGA and hybrid functionals are nowadays the most popular electronic-structure methods.

3.1.2 Dispersion corrected DFT

One of the main problems of standard DFT is its inability to describe the long-range dispersion interaction; both LDA and GGA local (sometimes described as semi-local) functionals. The dispersion interaction originates from the interaction of instantaneous dipoles formed due to correlated motion of electrons in the interacting molecules. The leading term of the dispersion interaction asymptotically scales as r^{-6} (r is the interatomic distance), followed by terms scaling as the r^{-n}, n = 8 and 10. There are several approaches to account for the dispersion interaction in DFT ranging from empirical corrections to new non-local functionals. The simplest method to add dispersion is through empirical correction to the DFT energies. The best known such correction is the Grimme's DFT-D scheme[41], which reduces the dispersion to pairwise contributions with an r^{-6} scaling with the distance and empirical C_6 atom-pair dependent parameters. The damping function is also added to avoid divergence for short distances. The revised functionals DFT-D2 and later DFT-D3 significantly increased the applicability of the DFT-D scheme. DFT-D2 added parameters for atoms up to Xe and most of the original C_6 coefficients and other parameters from DFT-D were refitted, yielding significant improvement in accuracy.[42] The scheme was then significantly revised in DFT-D3, including major changes like incorporation of the C_8 parameters.[43] Despite the strong empirical character of the DFT-D2 and D3 correction schemes they perform reasonably well for a variety of systems and they are currently the most popular choice for systems with significant dispersion interactions. Another type of the empirical correction for the dispersion can be shown on DFT/CC approach,[44] which is based on adding a set of pairwise corrections to the DFT interaction energy. These corrections are not universal but rather developed separately for each system on a set of reference molecules and are defined as a difference between the DFT and CCSD(T) energies built as a distance dependent kernel.

The non-local effects can be also described directly using costly methods like symmetry adapted perturbation theory, or using non-local DFT functionals. The first computationally affordable non-local DFT functional was vdW-DF functional from Rutgers-Chalmers.[45] This functional directly contains a non-local correlation energy term E_c^{nl} defined as the interaction of electron densities ρ over a non-local correlation kernel Φ;

$$E_c^{nl} = \frac{1}{2}\iint \rho(r)\Phi\,(r,r')\rho(r')drdr'. \quad (3)$$

There is a large number of non-local functional differing mainly in the selection of exchange and correlation functional upon which the non-local function was built. The original vdW-DF functional was based on the revPBE functional.[46] However, accuracy of the original vdW-DF is inferior to the empirical dispersion schemes like DFT-D. The original vdW-DF functional was later reworked in several directions, leading to functionals like VV10[47] or reworked version of the original functional named vdW-DF2,[48] which is based on the rPW86 functional.[49] The overall accuracy of these functionals is comparable to DFT-D3 methods without the necessity of large number of empirical parameters, which makes them preferred methods for the description of systems with significant dispersion interactions.

3.1.3 Calculation details

Majority of calculations reported in this thesis were performed using DFT methods introduced in previous chapters. The calculations featuring the periodic models of materials were performed in VASP program suite[50-53] using PBE,[38] PBE+D3[43], or vdW-DF2[48] functionals; the selection of functionals is reported in individual subchapters. A projector augmented wave approximation (PAW) and a plane wave basis set were used in all calculations. The energy cut-off was set to 400 eV for calculations with zeolites and constant unit cell (UC) parameters, to 600 eV for calculations with MOFs and to 800 eV in all calculations in which the UC parameters were optimized. The Brillouin-zone sampling was limited to Γ-point in all calculations, due to large UC size of the studied microporous materials. The calculations with cluster models were performed in Gaussian 09 program[54] using B3LYP hybrid functional[35]. Triple-zeta polarized basis set was used in most calculations used, *e.g.* the Schäfer basis set TZVP[55] (details reported separately for individual systems). The calculations with force field were also used for some zeolites with large UC; the calculations were performed in GULP program[56, 57] and the SLC force field.[58]

The powder diffraction pattern simulations for the ideal crystal structures were performed in Mercury CSD program[59] and the powder diffraction patterns for the finite sized crystallites with UDskip algorithm.[60] The CO stretching frequencies were calculated using the ω_{CO}/r_{CO} correlation method[61], which allows to predict the CO frequencies ν_{CO} based on the DFT optimized CO bond lengths:

$$\nu_{CO}[cm^{-1}] = ar_{CO}[\mathring{A}] + b + \Delta\nu + \Delta\omega, \tag{4}$$

where a and b are parameters obtained from the linear interpolation of CCSD(T) predicted frequencies and DFT geometries for a training set of molecules[61], $\Delta\nu$ is an anharmonicity correction, and $\Delta\omega$ is a correction for the difference between the training set and zeolite 1-T model. This method allows quick prediction of the frequencies with precision of few cm^{-1} only from cheap DFT geometry optimizations. The transition states in the investigations of chemical reactivity were optimized using several algorithms; namely optimization to the transition state using Berny algorithm or quadratic synchronous transit QST2 and QST3,[62] both implemented in Gaussian[54] for cluster models, and dimer[63] and nudged elastic band algorithms[64] as implemented in VTST tool for VASP program[65] for periodic models.

3.2 Models

Many microporous materials like zeolites or MOFs have a very well defined crystalline structure. Thanks to that they can be represented by a model of periodically repeating unit cells. Due to a small size of micropores (< 2 nm) the unit cells are usually small enough to use quantum chemistry methods, DFT methods in particular. The area of the micropore surface (inner surface) is distinctively larger than the external surface of zeolite crystals, even by several orders of magnitude (except for nanosized crystals). Therefore their external surface can be neglected and a periodic model approximating the structure by an infinite three-dimensional array of unit cells is a very reasonable model for microporous materials. The presence of micropores, however, brings issues that have to be addressed during the selection of a suitable method and model of the material. One of the main issues is the confinement effect of the pores, which completely surround any adsorbed molecules. The dispersion thus has a very significant role in adsorbate/adsorbent interactions and the use of dispersion corrected functionals or non-local functionals is necessary to properly describe the adsorption.

The representation of the crystal surface or defects in the structure is also possible using the periodic models, but has to be often addressed by special adjustments. The crystal surface can be modelled using two-dimensional periodic models, but these are only rarely implemented in common computational codes. Standardly it is modelled by thin layers of the material separated by vacuum (wide enough to prevent interlayer interactions). This produces a formal 3D unit cell containing two material surfaces. Defects can be also introduced into periodic models of materials, ranging from single atom vacancies in some crystallographic positions to models of small mesopores. However, the periodicity of the model makes the defect to be repeated in each unit cell, which can bring large artefacts in the calculations due to too unrealistic structure. The size of the unit cell thus has to be tuned for defective materials, often increasing the cost of the calculations.

The size of periodic models limits the precision of the quantum chemical methods usable with them. An alternative, usable for the precise descriptions of localized phenomena, are cluster models modelling just specific parts of the material. The small size of cluster models enables the use of more advanced functionals, including hybrid functionals, perturbation theory or even coupled cluster depending on the model size. On the other hand, cluster models generally do not fully describe the investigated material, leading to a necessary compromise between cluster size and model precision. The most precise coupled cluster methods can be used only for models up to few tens of atoms, whereas larger models up to several hundreds of atoms can be described with perturbation theory or hybrid DFT functionals. Larger models with hundreds to thousand atoms and periodic models of the similar size are mostly studied using GGA or non-local DFT methods.

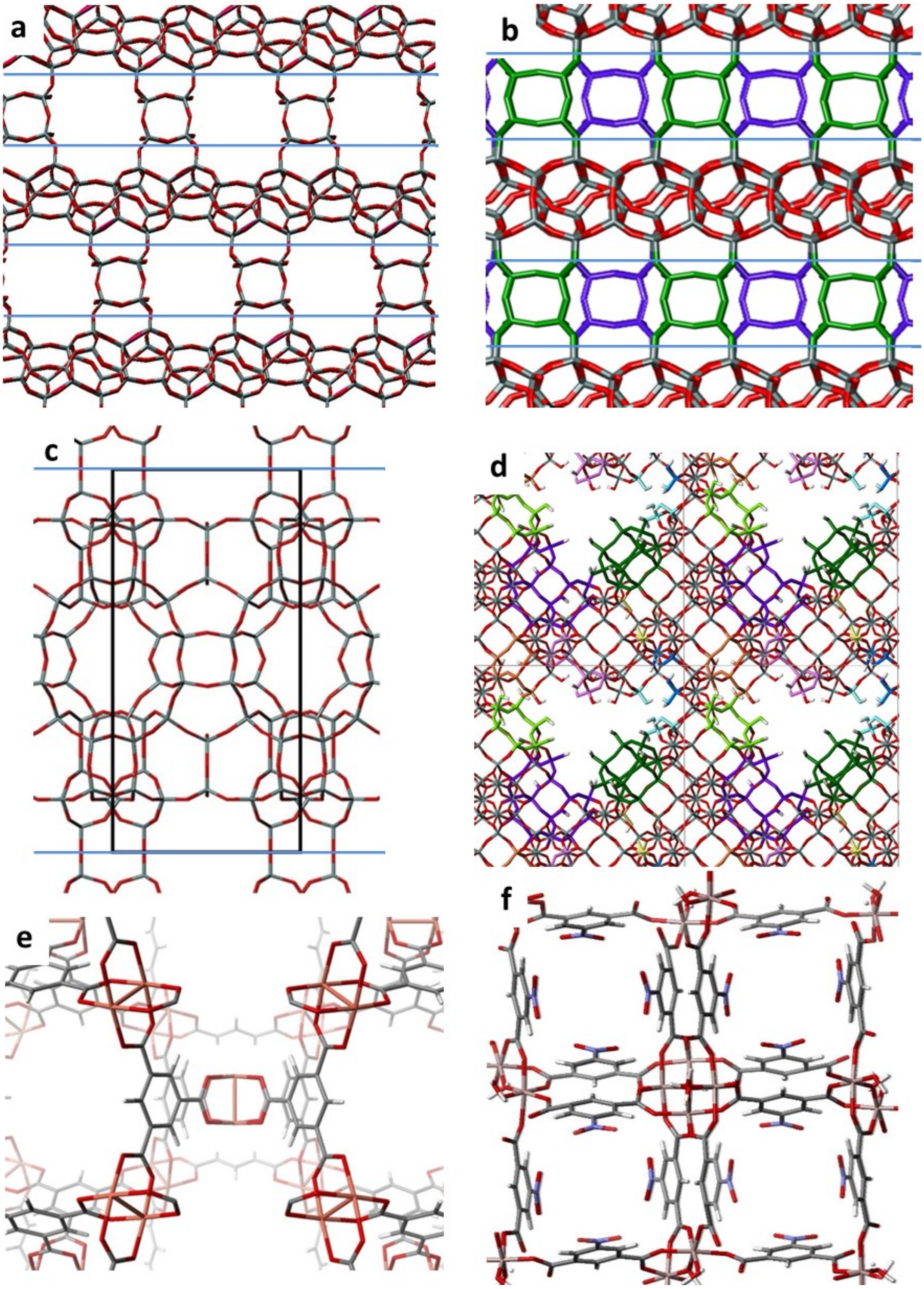

Figure 3.1 – a) UTL zeolite, blue lines delimit the IPC-1P layer structure; b) SAZ-1 zeolite, blue lines delimit the SAZ-1P layer structure, blue and green D4R units denote equivalent positions of D4R; c) MWW zeolite, blue lines delimit the MCM-22P layers; d) hierarchical USY model obtained by removal of fourth of T-atoms from FAU zeolite structure; e) CuBTC MOF; f) CAU-10-NO_2 MOF. Colour scheme: a-d – O in red, Si in grey, other colours denote special positions; e-f – O in red, C in grey, H in white, N in blue, Cu in pink, Al in light brown

3.2.1 Model details

Structures of following microporous materials were investigated (Figure 3.1); layered zeolite IPC-1P (UTL framework) and zeolites derived from it, layered zeolite SAZ-1P (CFI framework) and zeolites derived from it, layered zeolites MCM-22P and MCM-56 (MWW framework), hierarchical zeolite USY (FAU framework), and metal organic frameworks CuBTC and CAU-10. All materials, including layered zeolites, were modelled using full periodic models. Cluster models were also used for hierarchical USY zeolite, CuBTC and CAU-10 to study their reactivity and catalytic activity. The following section comprises the structural information on the particular materials that were studied, together with other technical details referred to from the Results and Discussion.

UTL and IPC-1P zeolite family

The UTL[66] structure was adopted from the IZA database (Figure 3.1a),[5] and the IPC-1P structure of two interacting layers (2L structure) was adopted from the Ref. [67]. The structures of periodically interacting IPC-1P layers were obtained by the transformation of the 2L structure to a periodic one and fully optimized (full optimization includes optimization of atomic positions, UC shape, and UC volume). The IPC-1P unit cell contains just one layer of IPC-1P with the composition $Si_{30}O_{64}H_{8}$. The UC parameters of all IPC-1P structures (including structures with SDA) were reoptimized in every calculation. The structures of new potential ADORable zeolites (zeolites that can be obtained using ADOR strategy) were constructed from the interacting IPC-1P layers. For the final structures of ICP-4 and IPC-2 zeolites see ref [68] (Attachment A) and for IPC-9 and IPC-10 structures see Ref. [69] (Attachment C).

SAZ-1 zeolite family

The basic SAZ-1[70] structure was adopted from the resolved structure of its analogue CIT-13.[71] The structure was subsequently modified to account for the disorder in the D4R arrangement and fully optimized. A UC containing two SAZ-1P layers with composition of $Si_{56}O_{112}$ was used, allowing four structures with different arrangements of D4R (Figure 3.1b, Table 3.1). The D4R in neighbouring UC can form either straight lines (denoted S in the Table 3.1) or zig-zag arrangements (denoted A in the Table 3.1).

The SAZ-1P layered zeolite was modelled using a periodic model of interacting layers. The layer structure was cut from the SAZ-1 zeolite structure and the surface was terminated by silanol groups. All SAZ-1P structures were fully optimized in each calculation. The structures of potential ADORable zeolites were also constructed from two possible SAZ-1P arrangements; the possible disorder in S4R was also considered for ADORable zeolites (see Table 3.1 for the details on UC size and parameters).

Table 3.1 –UC parameters of all zeolites in the SAZ-1 zeolite family.

	D4R/S4R DISORDER		Tat / UC	UC parameters					
material	intralayer *c-a* view[a]	interlayer *c-a* view[b]		a [Å]	b [Å]	c [Å]	α [°]	β [°]	γ [°]
SAZ-1	S-S	S-S	64	13.88	30.94	10.22	90.1	89.9	116.7
	S-S	S-A	64	13.89	27.66	10.23	90.2	90.0	90.0
	S-S	S-S	64	14.81	30.96	10.23	90.1	69.7	114.9
	S-A	S-A	64	14.81	27.65	10.24	90.1	69.8	90.0
CFI	no disorder		64	14.87	28.08	10.29	89.9	81.0	118.2
IPC-16	S-S	S-S	56	13.73	21.84	10.19	90.0	90.7	90.0
	S-S	S-A	56	13.83	21.96	10.23	90.5	90.6	90.6
	S-A	S-A	56	14.63	21.91	10.23	89.9	70.2	90.0
	S-A	S-A	56	14.71	21.98	10.23	90.6	70.2	90.8
SAZ-1-S4R_0.5c0a	S-S	S-S	56	13.19	21.04	10.26	89.3	89.7	89.9
	S-S	S-A	56	13.18	21.07	10.30	88.8	90.0	90.0
	S-S	A-S	56	13.12	21.37	10.12	90.0	89.2	90.2
	S-S	A-A	56	13.00	21.63	10.03	90.0	88.8	90.0
	S-A	S-S	56	14.13	21.08	10.28	88.6	68.7	89.5
	S-A	S-A	56	14.14	21.04	10.28	88.8	68.7	89.6
	S-A	A-S	56	14.14	21.29	10.19	89.7	68.5	89.8
	S-A	A-A	56	14.04	21.33	10.19	90.1	69.3	90.2
[c]	A-S	S-S	112	12.95	20.72	20.02	90.0	90.0	90.1
[c]	A-S	S-A	112	13.19	21.24	20.37	90.0	90.0	90.0
[c]	A-S	A-S	112	12.76	21.39	19.74	90.1	89.8	90.1
[c]	A-S	A-A	112	12.93	20.99	19.94	90.0	89.3	89.9
IPC-15	no disorder		48	14.00	17.38	10.20	89.9	89.9	89.5
SAZ-1-D4R_0.5c0a	no disorder		48	13.60	17.26	10.14	90.1	90.1	89.9

[a] Arrangement of the D4R/S4R in one interlayer region as viewed along *c* and *a* vectors (A arrangement along *c* is possible only for shifted zeolites)

[b] Arrangement of the D4R/S4R on opposite sides of the SAZ-1P layer as viewed along *c* and *a* vectors (A arrangement along *c* is possible only for shifted zeolites)

[c] UC parameters obtained from the FF (SLC force field)[58] calculations instead of PBE due to the size of UC

MCM-22P and MCM-56 layered zeolites

The structure of MWW layers was derived from the parent MCM-22 zeolite[72] simply by cutting the crystal along the plane with the lowest density of T–O–T links and terminating surfaces with OH groups (Figure 3.1c). The resulting UC has a composition $Si_{72}O_{146}H_4$. The periodic model of interacting layers was used and all structures were fully optimized in each calculation. The theoretical powder XRD patterns were simulated for the structures obtained at the vdW-DF2 level. The pXRD patterns were calculated with finite-size crystals using the UDskip software.[60, 73] The wavelength of 1.5418 Å (CuKα) and crystals of the size 30 × 30 × 30 UC were used, which corresponds to crystal dimension about 40 × 40 × 80 nm. The disorder in the layer arrangement (described in detail in Chapter 4.1.3) was simulated as follows: *c* vectors defining the arrangement for each pair of neighbouring layers were randomly selected from the pool of allowed c vectors and 30 × 30 × 1 UC layers were combined in this way into the final 30 × 30 × 30 UC crystals. This procedure was repeated and the superposition of the simulated XRD patterns was obtained to ensure good statistics. The randomized structures were not reoptimized.

Hierarchical USY zeolite

The FAU structure was taken from the IZA database.[5] The mesopore was introduced by removing of 49 out of 192 T-atoms from the primitive FAU unit cell to form a hierarchical USY (siliceous model of FAU, Figure 3.1d). First, three out of four D6Rs composite building units in one sodalite cage were removed to create a cavity within the framework. Second, additional framework atoms were removed to define various types of possible defects. Following sites were defined (Figure 3.2).: The remaining D6R unit of this sodalite cage represents the S_{D6R} site. For each removed D6R site, a sodalite cage opening was exposed, denoted S_{06R}. For one of those sites, additional framework SiO_2 units were removed to form surface six-membered ring S_{S6R} site. Subsequently, the defect sites S_{-1T} and S_{-2T} were constructed by a removal of one or two T-atoms bearing silanol groups from one of the S_{06R} sites, respectively. The last model defect site was obtained by removal of an individual T-atom from the zeolite wall. All unsaturated oxygen atoms were terminated with H atoms forming surface silanols and the final geometry was optimized. The resulting model of hUSY has the following composition and UC parameters: $Si_{143}O_{309}H_{46}$, a = 24.55 Å, b = 24.53 Å, c = 24.56 Å, α = 90.0°, β = 90.1°, γ = 90.0°.[74]

The cluster models representing each surface site were also used. The cluster geometry was taken from the optimized periodic model and constrained to maintain the original structural features as shown in Figure 3.2. Only atoms represented by balls in the Figure 3.2 were relaxed during geometry optimizations. The O-Si bonds on the cluster edge were replaced by O-H bonds with the original direction and length of 1.05 Å. A 12T Na-FAU model was also used as a model of standard FAU zeolite with single Na^+ ion placed in type II site. A model of periodic FAU terminated with surface six-membered rings S_{S6R} was also used for the investigation of the reaction mechanisms with periodic catalyst model. The composition of this model was $NaH_{11}Si_{54}O_{114}$ and UC parameters a = c = 17.372 Å, b = 35.0 Å, α = β = γ = 60°.

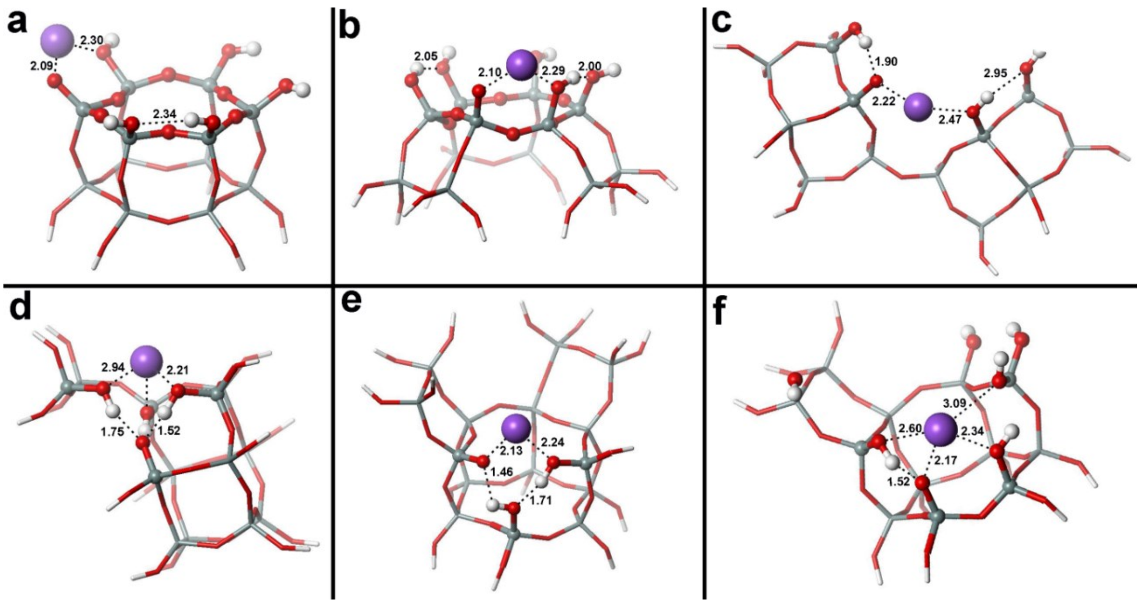

Figure 3.2 – Cluster models of the Na-hUSY active sites; clusters were cut from the previously optimized periodic model and partially frozen to respect the framework rigidity. Only atoms depicted as balls were fully relaxed during the geometry optimization. a – S_{D6R} site, 12T cluster model; b - S_{S6R} site, 12T cluster model; c – S_{06R} site, 12T cluster model; d – B_{-1T} site, 13T cluster model; e – S_{-1T} site, 15T cluster model; f – S_{-2T} site, 13T cluster model. Distances in Å. Si, O, H and Na atoms depicted in grey, red, white and purple, respectively. Colour scheme: grey, red, white and purple for Si, O, H and Na, respectively. Reproduced with permission from Ref.[74] Copyright 2016 American Chemical Society.

CAU-10-NO_2 metal organic framework

The geometry of CAU-10-NO_2 MOF[75] was optimized using a periodic model with the UC parameters fixed to experimentally determined values (a = b = 21.4647 Å, c = 10.3751 Å, $\alpha = \beta = \gamma = 90°$, Figure 3.1e). Calculations of electronically excited states and calculations with the anion-radical were performed with the $Li_2C_6H_3(COO)_2NO_n$ (n = 1 and 2) cluster model, the geometry of which was constrained to the geometry obtained with the periodic model; only the position of the Li^+ ions and the NO or NO_2 group were relaxed.

CuBTC metal organic framework

Two models of CuBTC[25] were used in the investigation of the reaction mechanism: the periodic and the cluster model. The periodic structure of CuBTC was represented by the reduced rhombohedral unit cell of CuBTC (a = b = c = 18.774 Å and $\alpha = \beta = \gamma = 60°$, volume 4679 $Å^3$), with composition $Cu_{12}O_{48}C_{72}H_{24}$ (Figure 3.1f). The cluster model used consisted of two paddlewheel units interconnected by phenylene group and terminated by hydrogens $[(HCOO)_3Cu_2(OOC\text{-}C_6H_4\text{-}COO)Cu_2(HCOO)_3]$. Initial geometry of the cluster was taken from the periodic model and all geometry optimizations were performed with partially constrained geometry (only Cu atoms interacting with adsorbents, all carboxylate groups in one paddlewheel and top oxygen atom in the other paddlewheel were optimized).

4. Results and Discussion

4.1 Structure of new zeolites

4.1.1 UTL and IPC-1P zeolite family

Background

UTL is a germanosilicate with a 2D channel system of perpendicular interconnected 14- and 12-membered ring channels.[66] The UTL framework consists of the layered blocks interconnected via double-four membered rings (D4R), which are the preferential sites for the Ge atoms. That makes D4R prone to hydrolysis, upon which siliceous layered zeolite IPC-1P was obtained (Figure 3.1a).[76] One of the most interesting post-synthetic modifications that can be done with IPC-1P is the possibility of reconnecting the layers. Unlike in other known layered zeolites, the reassembly of IPC-1P layers does not lead to the parent zeolite UTL, but rather to a new zeolite IPC-4. Furthermore, another new zeolite can be prepared by interlayer expansion of the IPC-1P layers by silica (see Chapter 2.2 for more details on interlayer expansion), leading to another new zeolite called IPC-2. The main task of this theoretical study was to identify the structure of IPC-1P and of the new zeolites that can be obtained from it.[68]

The structure of IPC-1P layers was previously studied by Grajciar et al,[67] using a model of IPC-1P bilayer. IPC-1P has a relatively high concentration of surface silanols (1 silanol per 43 Å^2), arranged in quadruplets on the IPC-1P surface. The distances between the silanol groups (circa 5 Å inside quadruplets and 7-8 Å between quadruplets) enable several layer arrangements, differing in a shift of the layers along in-plane (*b* or *c*) crystallographic direction. Grajciar et al discovered four optimal layer arrangements; two structures corresponding to the unshifted layer arrangement similar to UTL differing in the direction of hydrogen bonds; and structures with one layer shifted by half of the unit cell along *b* or along *c* vector. The layer arrangement corresponding to the original UTL structure is the most stable of them, with the preference of 10 kJ mol^{-1} to all other arrangements (see Table 4.1).[67]

Layered zeolite IPC-1P

The herein reported study directly followed the previous work by Grajciar et al.[67] A more realistic model of IPC-1P material representing an infinite stack of 2D layers was used. Both PBE and vdW-DF2 functionals were used during the investigation to evaluate the role of dispersion on the layer interaction. The PBE results for periodically interacting layers are very similar to a model of two interacting layers (2L model) (Table 4.1). However, the vdW-DF2 functional results differ distinctively, which is caused by a change in the shape of individual IPC-1P layers due to strong dispersion interaction. The layer arrangement corresponding to the original UTL structure is still the energetically most stable one but the relative energies of structures shifted along ±*c* decreased from 50 to 25 kJ mol^{-1}.

Table 4.1 – Relative energies of different IPC-1P layer arrangements for periodically interacting layers and bilayer. Bilayer data adopted from ref[67]. All energies are in kJ mol^{-1}.

	periodic		bilayer (Grajciar et al[67])	
structure[a]	E_{rel} (PBE)	E_{rel} (vdW-DF2)	E_{rel} (PBE)	E_{rel} (vdW-DF2)
IPC-1P_0_0_eps	0	5	0	0
IPC-1P_0_0_-eps	3	0	11	13
IPC-1P_0_-eps_0	26	8	31	11
IPC-1P_0_eps_0.5	53	25	49	38
IPC-1P_0_-eps_0.5	52	25	58	45
IPC-1P_0_0.5_eps	14	9	19	11
IPC-1P_0_0.5_-eps	20	11	17	9

[a] The structure names indicate layer shifts along UC vectors in sequence (IPC-1P)_*a*_*b*_*c*; eps stands for the small layer shift caused by the interlayer hydrogen bonds and denotes the direction of hydrogen bonding.

Zeolites IPC-4 and IPC-2

The formation of the zeolite IPC-4 was modelled by a direct reconnection of IPC-1P layers, forming oxygen bridges in-between the layers. Four possible IPC-4 zeolite structures were considered, corresponding to the layer arrangement from the original UTL zeolite and structures with layers shifted by a half a unit cell along *b* and/or *c* direction. The unshifted layers produce zeolite with 10 x 8 ring channel system, the shift along *b* direction produces 8 x 8 ring channels, while shift along *c* leads to 10 x 7 ring channels, and a combination of both shifts gives 8 x 7 ring channel system. (Figure 4.1). The existence of four possible zeolites differing in the layer shift is quite similar to the already known family of zeolites FER and CDO, which are both derived from ferrierite layers and differ in the layer shift (see Chapter 2.2). The layer arrangement directly obtained from the UTL zeolite (derived from IPC-1P_0_0_±eps) is the most stable structure by more than 100 kJ mol^{-1} (at PBE level). Powder X-ray diffraction (pXRD) patterns of all potential zeolites were also simulated and compared with experiment; unshifted structure provides the match with the experimental pXRD pattern. IPC-4 was thus identified as a new zeolite with 10-ring channels parallel to the *c* axis and 8-ring channels parallel to the *b* axis, which was also confirmed by Rietveld refinement.[68]

IPC-2 structural model was created similarly to the IPC-4 zeolite, but the layers were linked with the O-Si-O bridges to model the layer expansion by added silica. Analogously to D4R in UTL, the silicon bridges can form single-four membered rings (S4R). Therefore, no silanols are present on the silicon bridges and the resulting material is a zeolite by definition (it fulfils the full connectivity criteria), unlike interlayer expanded materials formed from MWW or FER zeolites. The resulting material has a similar topology as IPC-4 but with larger channels; unshifted zeolite has 12 x 10 ring channels, the shift along *b* produces 10 x 10 ring channels, the shift along *c* produces 12 x 9 ring channels, and combination of both shifts gives 10 x 9 ring channels (Figure 4.2). Similarly to IPC-4 zeolite, the structure with unshifted layers and 12 x 10 channel system was found to have the lowest energy as well as the best match with the experimental data.

The DFT simulated structures of IPC-2 and IPC-4 zeolites and also IPC-1P were also used as the starting structures to interpret the experimental pair distribution function analysis.[77] The results for IPC-2 and IPC-4 zeolite show an excellent fit between the models and experimental data, confirming the structure of both zeolites. The IPC-1P_0_0_±eps structure also had a reliable match with the experimental data; however, the results show some level of disorder in the layer arrangement that can be assigned to either some population of other shifts or to the presence of some already condensed layers of IPC-2 or IPC-4 zeolite. More information is provided in Attachment B.

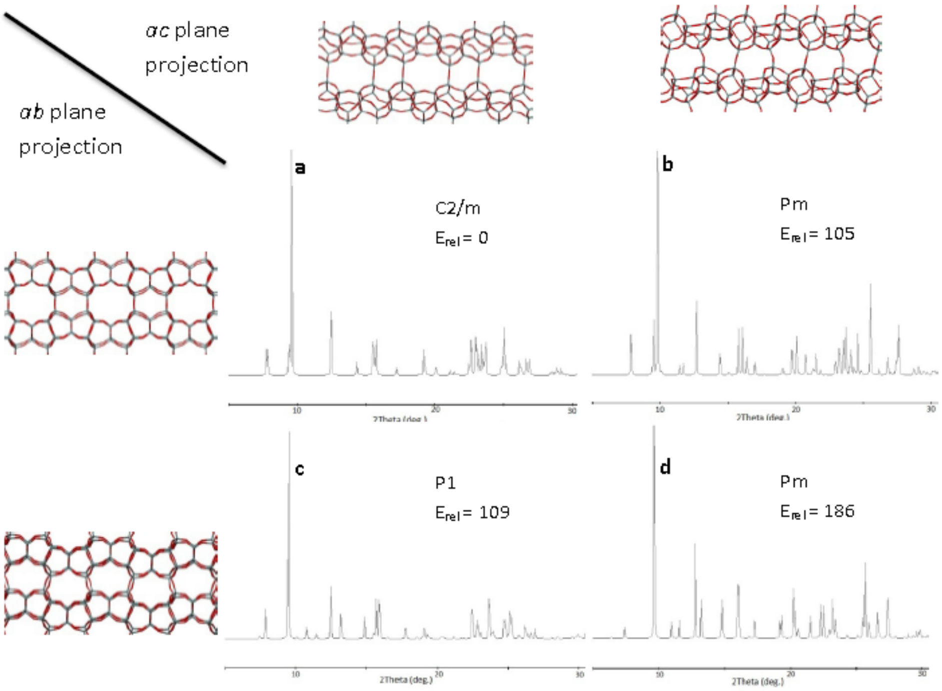

Figure 4.1 – Structures and simulated powder diffraction patterns for the four possible zeolites formed by the direct calcination of IPC-1P layers with different interlayer shifts. IPC-4 zeolite pattern is depicted top-left. Reproduced from the supplementary information of Ref.[68]

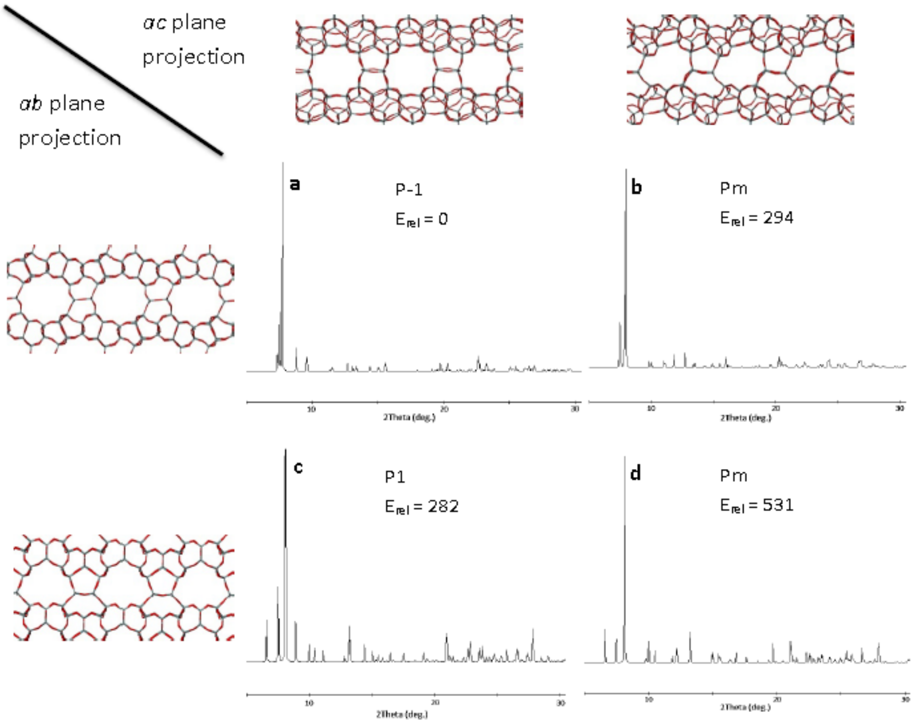

Figure 4.2 – Structures and simulated powder patterns for the four possible inter-layer expanded zeolites obtainable from IPC-1P layers with different interlayer shifts. IPC-2 zeolite pattern is depicted top-left. Reproduced from the supplementary information of Ref.[68]

The use of organic SDA during the IPC-4 zeolite synthesis significantly improves quality of the final material. Octylamine was found to be particularly suitable for the layer organisation. The influence of octylamine was therefore studied computationally with an IPC-1P 2L model and vdW-DF2 functional. The addition of the SDA molecule significantly enhances the preference for the IPC-1P_0_0_±eps arrangement, increasing the relative energy of other structures to more than 30 kJ mol^{-1}. Also the IPC-1P_0_-eps_0 structure, proposed by Grajciar et al.,[67] is destabilized due to the octylamine preference for the 10-ring channel, which are blocked by silanols in this arrangement. This may contribute to the effect of SDA on the layer ordering during the IPC-4 synthesis.

The herein reported results were published in ref [68] together with the experimental results describing the IPC-2 and IPC-4 synthesis. This publication is attached to this work as Attachment A. The overall IPC-4 formation procedure was called ADOR, standing for Assembly of the original UTL zeolite, its Disassembly to the IPC-1P layers, Organization of the layers by SDA and finally Reassembly of the layers to a new zeolite structure. The IPC-4 zeolite was approved by IZA under the code PCR, whereas the IPC-2 was found to be isostructural with the zeolite OKO.[78]

Zeolites IPC-9 and IPC-10

The synthesis of IPC-2 and IPC-4 zeolites promoted the investigation of other theoretically predicted zeolites in the IPC-1P zeolite family. Recently, a pair of new zeolites IPC-9 and its expanded analogue IPC-10 was discovered, which were identified by pXRD as zeolites produced by shift of the IPC-1P layers along *c* vector (top right structure in Figures 4.1 and 4.2).[69] The key step in the IPC-9 and 10 syntheses is the reorganization of the IPC-1P layers, which requires breaking of the hydrogen bonds between the layers. Two reorganization experimental procedures were found, either swelling of the layers by large surfactants or deprotonation of the silanol layer by basic conditions, both of them followed by the intercalation of SDA between the layers. Choline cation was found to be particularly effective as SDA for the layer shift. The aim of the study was to investigate and explain the role of choline in the reorganization of the layers.

The experimental conditions are sufficiently basic to deprotonate a part of surface silanols on IPC-1P to form silanolates. The resulting charge of the surface is compensated by choline cations. The preferential adsorption sites of choline cation on the IPC-1P surface were identified in the first step of investigation. There are three possible adsorption sites for choline; i) pocket between the silanol quadruplets in the place of original 12R channel, ii) pocket in the place of original 14R channel, and iii) channel intersection (Figure 4.3). The adsorption of one and two choline cations per silanol quadruplet was studied at the vdW-DF2 level; water solvent was not taken into account. The preferential adsorption site of the first choline cation at the silanol quadruplet is the 12R channel pocket (Table 4.2, Figure 4.3), while the second cation is adsorbed in 14R channel pocket. The adsorption in the channel pockets maximizes the interaction of the large cation with the zeolite surface as well as interaction of choline hydroxyl groups with the silanolates. Interaction energies calculated at the vdW-DF2 level for the first and the second choline molecules were 168 and 201 kJ mol^{-1}, respectively.

Table 4.2 – Relative energies of choline cation interacting with charged IPC-1P surface at the vdW-DF2 level

choline position	E_{rel}[a]
12R channel pocket	0
14R channel pocket	7.1
12R/14R intersection (along 12R channel)	38.8
12R/14R intersection (along 14R channel)	30.4

[a] In kJ mol^{-1}.

The periodic model of an infinite stack of IPC-1P layers was employed for the investigation of the choline effect on the layer stacking. The IPC-1P layers with choline already present in the preferential adsorption sites were used to build the crystals. The adsorption of 2 and 4 choline cations per UC was thus considered, corresponding to 1 and 2 choline cations per silanol quadruplet, respectively. All four possible IPC-1P layer arrangements corresponding to predicted zeolite structures were investigated. As most stable without any SDA. However, when just one silanol in each quadruplet is

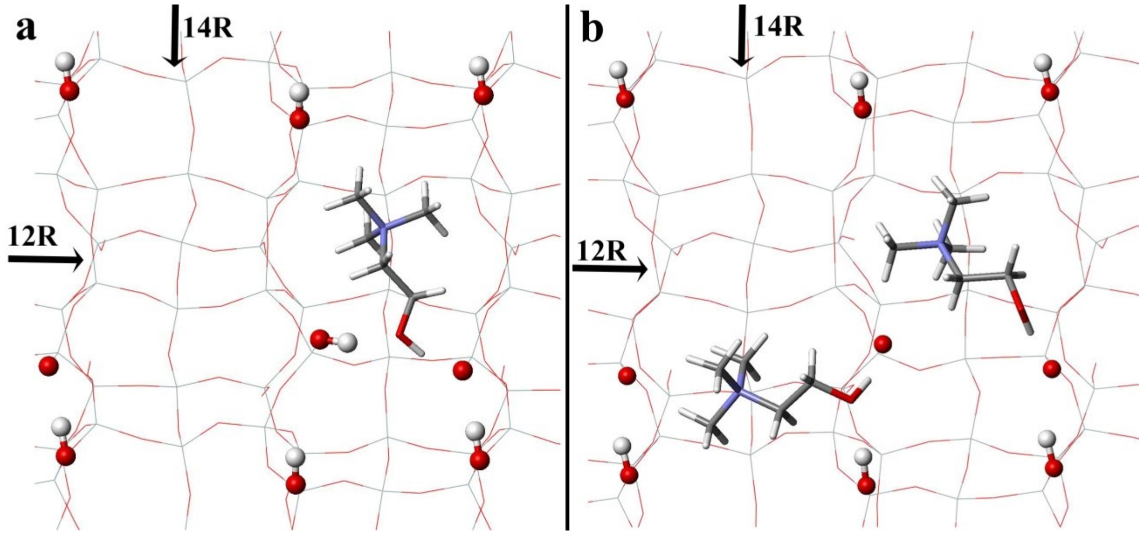

Figure 4.3 – IPC-1P single-layer with one (a) and two (b) choline cations adsorbed in the energetically most preferable positions: a) choline cation in 12R channel pocket, b) choline cations in 12R and 14R channel pockets. Colour scheme: O in red, H in white, N in blue, C as grey stick and Si as grey wireframe. Reproduced form supplementary information of Ref. [69]

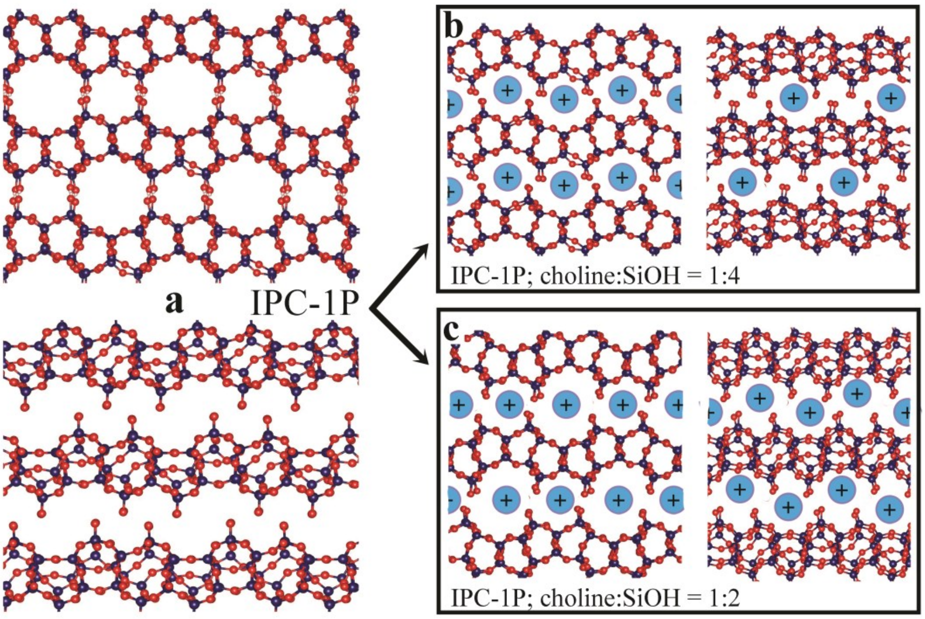

Figure 4.4 – Schematic representation of the IPC-1P layered zeolite without and with choline cations as SDA; a) IPC-1P in the original arrangement, b) IPC-1P with two choline cations per UC, layers shifted along *b* direction, c) IPC-1P with four choline cations per UC, layers shifted along c, precursor of IPC-9 zeolite. Colour scheme: O in red, Si in dark blue. Adapted from Ref. [69]

deprotonated (simulating high pH) and choline cation is added, the strong electrostatic reported above, the IPC-1P_0_0_eps structure, corresponding to zeolite IPC-4, is the repulsion of the negatively charged silanol quadruplets forces the layers to shift (Figure 4.4). The structure shifted along the *b* vector with one choline per silanol quadruplet present is energetically preferred, whereas the original layer arrangement is 100 kJ mol^{-1} higher in energy (Table 4.3). Nevertheless, the shift along *c* becomes the most preferred at high choline coverage (4 cholines per UC), leading to zeolite IPC-9 (Figure 4.4).

Table 4.3 – Relative energies of different IPC-1P inter-layer arrangements with 0, 2, and 4 choline cations in UC calculated at the vdW-DF2 level of theory.

Structure		Shift along b	Shift along c	E_{rel}[b]		
Zeolite	IPC-1P[a]			0 chol$^+$	2 chol$^+$	4 chol$^+$
IPC-1P-10R/8R (IPC-4)	IPC-1P_0_0_eps	no	no	0.0	103.0	164.7
IPC-1P-10R/7R (IPC-9)	IPC-1P_0_eps_0.5	no	yes	24.8	21.5	0.0
IPC-1P-8R/8R	IPC-1P_0_0.5_eps	yes	no	8.7	0.0	82.5
IPC-1P-8R/7R	IPC-1P_0_0.5_0.5	yes	yes	-	58.3	-

[a] see Table 4.1
[b] In kJ mol^{-1}

The zeolite IPC-10 is obtained by the interlayer expansion of IPC-1P layers by silica and an introduction of S4R groups, similarly to the IPC-2. Dense layers of IPC-1P are arranged in IPC-10 exactly in the same way as in IPC-9 (shifted along *c* vector). However, S4Rs formed between the dense layers can have several possible arrangements, because the S4R can be created with the same probability in each of the two identical 7-membered rings of IPC-9 UC. In a projection to *ac* plane, either 5-membered or 6-membered rings formed between the S4R and IPC-1P layer (Figure 4.5). The S4Rs on opposite sides of one layer can be connected either both via 5R, or both via 6R or each side differently. Two possible IPC-10 geometries are thus defined (Figure 4.5); i) structure with a repeating motif of layers with both 5R and 6R (resulting in Pm symmetry, UTL-S4R(Pm)); ii) structure with alternating 5R/5R and 6R/6R layers (resulting in P-1 symmetry, UTL-S4R(P-1)). The UTL-S4R(P-1) is 2 kJ mol^{-1}(SiO$_2$)$^{-1}$ energetically below the UTL-S4R(Pm) structure. Nonetheless, the energy difference is quite small, resulting in the possible disorder in the IPC-10 structure. This possible disorder could explain the generally worse resolution of IPC-10 pXRD patterns.

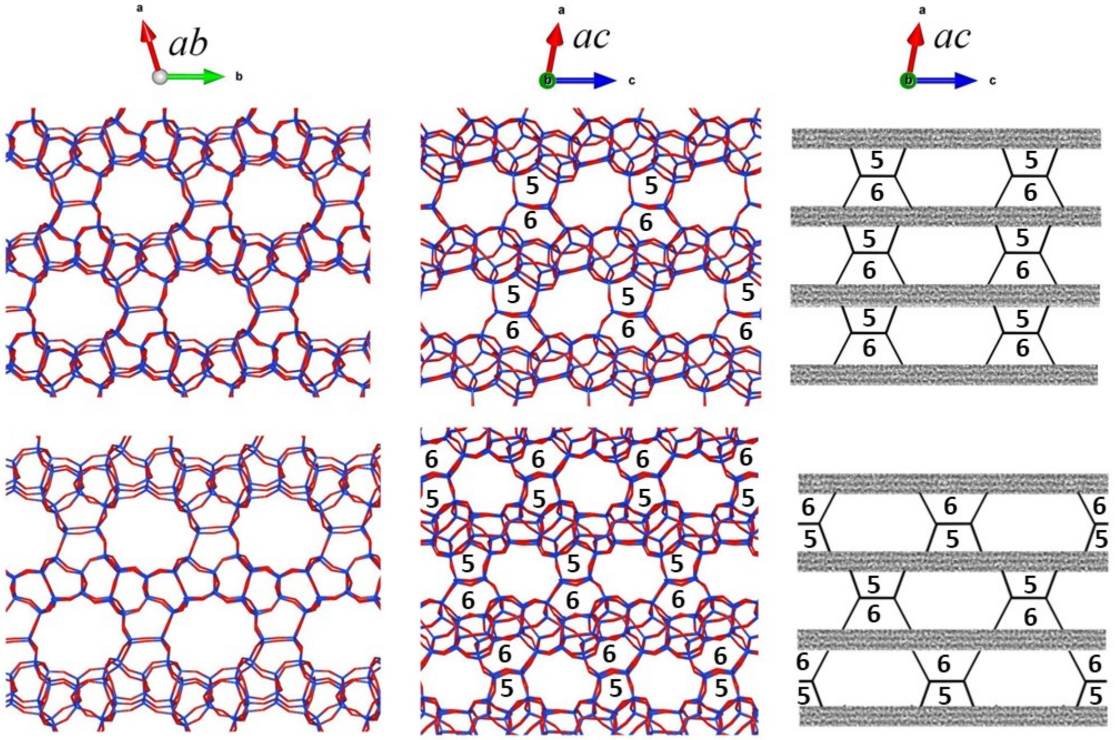

Figure 4.5 – Comparison of UTL-S4R(Pm) (top) and UTL-S4R(P-1) (bottom) as two possible structures of IPC-10 zeolite; projection along c (left) and b (middle) crystallographic directions and a schematic representation of both structures (right). Positions of 5M and 6M rings between S4R and IPC-1P layers highlighted. Si and O depicted in blue and red, respectively. Adapted from Ref. [69]

The feasibility criteria of many hypothetical ADOR zeolites, including IPC-9, were evaluated by Trachta et al.[79] The same was repeated herein for all different S4R arrangements, which were not considered before. Two main criteria were evaluated; feasibility factor[7] and LID criteria[9] (Table 4.4). The feasibility factor ϑ expresses how far is the hypothetical zeolite from the optimal energy-density ratio of known zeolites (see Chapter 2.1 and Figure 2.1). The ϑ value of IPC-9 and IPC-10 reaches 1.7 and 4.9, respectively, indicating they are rather unfeasible for conventional synthesis. The other evaluated feasibility criterion is LID criteria (see Chapter 2.1). Both PC-9 and IPC-10 do not obey at least one LID criterion and thus they have to be considered unfeasible zeolites. However, both feasibility factor and LID criteria were developed for the standard solvothermal synthesis, whereas ADOR strategy starts from the already formed zeolite blocks. The IPC-9 and IPC-10 thus show that ADOR strategy can lead to zeolites that are considered inaccessible by standard methods. The herein reported theoretical study of the IPC-9 and IPC-10 zeolites was a part of combined experimental and theoretical investigation reported in Ref. [69] that is included in this thesis as Attachment C.

Table 4.4 – The values of framework energies and framework densities (calculated using both vdW-DF2 and SLC force field) for zeolites IPC-9 and IPC-10. Also listed is the ϑ, the feasibility factor and whether the material passes or fails the LID criteria (1 = pass, 0 = fail). For comparison the values for zeolites with the OKO and PCR topologies are also listed.[79]

	$FE_{DFT}{}^{a}$	$FE_{FF}{}^{a}$	$FD_{DFT}{}^{b}$	$FD_{FF}{}^{b}$	ϑ	LID criteria				
						1	2	3	4	5
PCR	9.1	10.4	18.1	19.3	1.4	1	1	1	1	1
OKO	11.2	13.8	17.0	17.8	0.5	1	1	1	1	1
IPC-9	12.5	14.0	18.7	19.8	1.7	0	1	1	0	1
IPC-10	16.8	20.1	18.0	18.8	4.9	0	1	0	0	1

4.1.2 SAZ-1 zeolite family

The success of ADOR strategy in the UTL zeolite family promoted the study of other known germanosilicates as possible sources of new zeolite structures.[79-81] Also, the synthesis of new germanosilicate networks is studied extensively as a source of new D4R containing zeolites.[82] Recently, a new germanosilicate zeolite was synthetized independently in three groups under the names CIT-13,[71, 82] NUD-2[83], and SAZ-1.[70] The solution of experimental zeolite structure showed that it is a D4R containing zeolite with layers similar to IPC-1P.[71] The SAZ-1 zeolite was subsequently investigated in prospects of ADOR strategy and two new zeolites, IPC-15 and its interlayer expanded analogue IPC-16, were successfully obtained. The structures of SAZ-1 and IPC-16 show a high degree of disorder which is strongly dependent on the synthetic procedure. The aim of the herein reported study was to identify the structures of IPC-15 and IPC-16 zeolites similarly to the previous investigation of IPC-1P derived zeolites and also investigate the nature of the disorder in the SAZ-1 parent zeolite.

The SAZ-1P layers can be found in an already existing zeolite framework CFI,[84] which is an SAZ-1P interlayer expanded zeolite with SAZ-1P layers connected via SiO_2 linkers forming the walls of 1D channels. The SAZ-1P layers are very similar to IPC-1P, but have larger concentration of surface silanols; 2.8 in SAZ-1P compared to 2.3 silanol/nm^2 in IPC-1P. Contrary to IPC-1P the distances between silanols in SAZ-1P are almost identical (Figure 4.6) and therefore there are multiple possibilities how to arrange D4R groups in SAZ-1. Consequently, there are two different D4R arrangements in the interlayer space between adjacent SAZ-1P layers; either aligned behind each other forming straight channels along *a* vector, or alternating forming zigzag channels (Figure 4.6). The same disorder can be found in the mutual arrangement of D4R on opposite sides of SAZ-1P layer. This disorder is very similar to disorder in the S4R arrangement in IPC-10 zeolite reported above (Chapter 4.1.1). In order to describe both intralayer and interlayer disorder, a SAZ-1 model UC containing two SAZ-1P layers was used to determine the SAZ-1 structure.

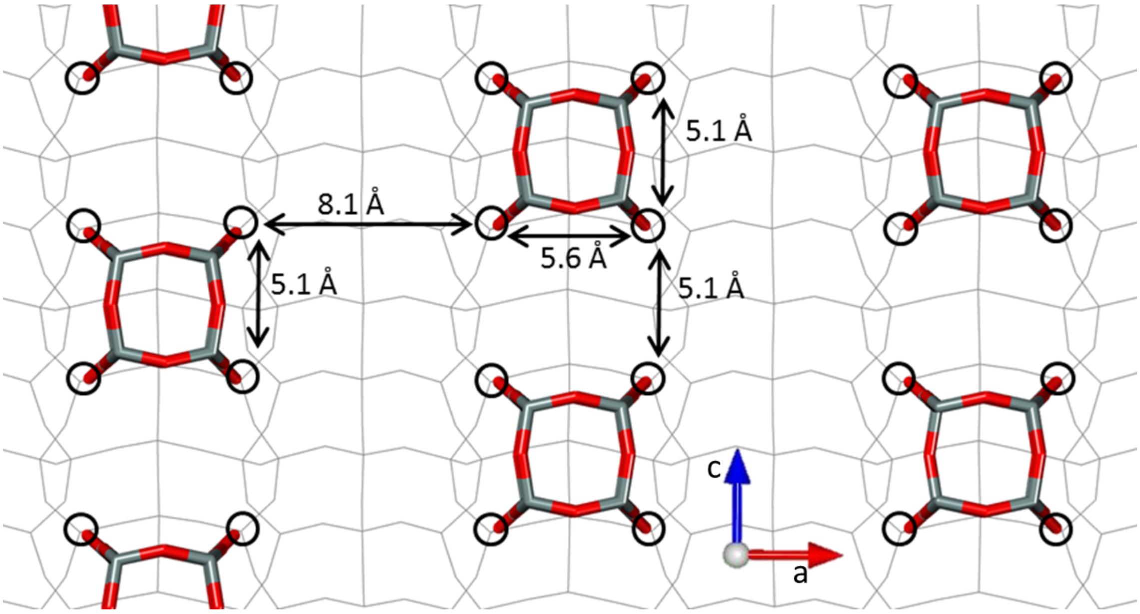

Figure 4.6 – Schematic representation of the irregularity in the D4R/S4R arrangement on the SAZ-1P layer surface. Black circles and distances denote positions of silanol groups on the SAZ-1P surface. The middle and right columns of D4R form straight lines along *a* vector, corresponding to the *S* arrangement; the left and middle columns of D4R form zig-zag lines along *a* vector, corresponding to the *A* arrangement. Colour scheme: O in red, Si in grey.

There D4R in SAZ-1 zeolite can be either perfectly aligned, forming straight rows on the surface along *a* direction, (denoted *S*), or alternating (denoted *A*), forming zig-zag lines (Figure 4.6). These two layouts can be found both for D4R arrangement inside one layer (intralayer disorder) and arrangement of D4R on the opposite sides of the layer (interlayer disorder); producing in total four possible SAZ-1 1 zeolite structures (Table 4.5, Figure 4.7). The structures and relative energies of the zeolites were investigated using PBE+D3 functional. Relative energies of a purely siliceous SAZ-1 are similar, with a small preference for the structure with straight channels in an interlayer region and D4R alternating across the layers. The energy differences are caused by a significant deformation of the SAZ-1P layers due to the strain induced by D4R.

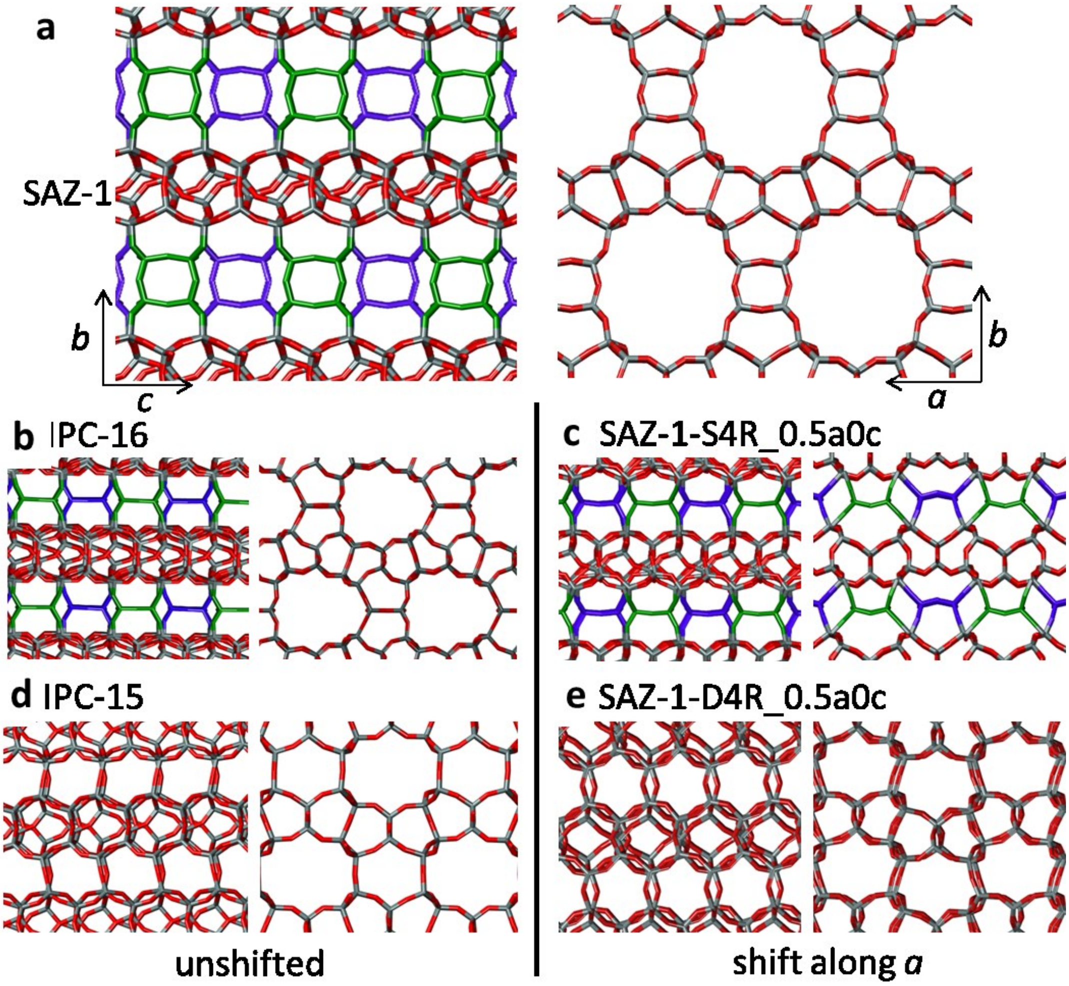

Figure 4.7 – a) structure of the SAZ-1 zeolite; b) and c) interlayer expanded zeolite IPC-16 and its analogue with shifted layers, respectively; d) and e) zeolite IPC-15 and its analogue with shifted layers, respectively. Possible dual D4R or S4R locations due to structural disorder denoted in blue and green in all relevant structures.

Structures of IPC-15 and IPC-16 were simulated analogously to the IPC-4 and IPC-2 as reported above in Chapter 4.1.1. The structures of interacting SAZ-1P layers were optimized to determine the possible shifts. Only one layer shift (along *a* vector) produces a symmetrically non-equivalent structure. The SAZ-1P layer arrangement

Table 4.5 – Relative energies (PBE+D3) and LID criteria of zeolites in SAZ-1 zeolite family.

	ring sizes		D4R/S4R DISORDER			LID criteria					
material	a	c	intralayer (*c*-)*a* view [a]	interlayer (*c*-)a view[b]	E_{rel}[c] per Tat	1	2	3	4	5	6
SAZ-1	10R	14R	S	S	0.3	1	1	1	1	1	1
			S	A	0	1	1	1	1	1	1
			A	S	0.1	1	1	1	1	1	1
			A	A	0.1	1	1	1	1	1	1
CFI	-	14R	no disorder		-1.3	1	1	1	1	1	1
IPC-16	8R	12R	S	S	0.6	1	1	1	1	1	1
			S	A	0	1	1	1	1	1	1
			A	S	0.2	1	1	1	1	1	1
			A	A	0.2	1	1	1	1	1	1
SAZ-1-S4R_0.5c0a	8R	10R	S-S	S-S	6.5	0	1	0	0	1	1
			S-S	S-A	5.4	0	1	1	1	1	1
			S-S	A-S	9.0	0	1	0	0	0	1
			S-S	A-A	6.7	0	1	0	0	1	1
			S-A	S-S	6.3	0	1	0	0	1	1
			S-A	S-A	5.7	0	1	1	0	1	1
			S-A	A-S	9.3	0	1	0	0	0	1
			S-A	A-A	8.9	0	1	0	0	1	1
			A-S	S-S	8.5	0	1	0	0	1	1
			A-S	S-A	9.3	0	1	0	0	1	1
			A-S	A-S	9.0	0	1	0	0	0	1
			A-S	A-A	9.1	0	1	0	0	1	1
IPC-15	6R	10R	no disorder		0	1	1	1	1	1	1
SAZ-1-D4R_0.5c0a	6R	8R/8R[d]	no disorder		2.1	1	1	1	1	1	1

[a] Arrangement of the D4R/S4R in one interlayer region as viewed along *a* direction (for unshifted zeolites) and both *c* and *a* directions (for shifted zeolites)

[b] Arrangement of the D4R/S4R on opposite sides of the SAZ-1P layer as viewed along *a* direction (for unshifted zeolites) and both *c* and *a* directions (for shifted zeolites)

[c] Energy per T-atom, in kJ mol^{-1}

[d] two identical channels per UC

corresponding to SAZ-1 zeolite is 18 kJ mol^{-1} per UC (at vdW-DF2 level) more stable than the shifted one, similarly to IPC-1P zeolite. Two potential structures of IPC-15 zeolite were then constructed by direct reconnection of SAZ-1P layers. The more stable, unshifted, structure (Table 4.5) agrees well with the experimental characteristics of IPC-15 zeolite. It is also important to note, that neither IPC-15 nor its shifted analogue contain the disorder similar to SAZ-1 due to the lack of pillaring groups in-between the layers.

The IPC-16 structure was constructed from IPC-15, analogously to the IPC-10 zeolite, by the interlayer expansion of SAZ-1P layers (in the unshifted arrangement) by S4R units. The structure of IPC-16 has similar disorder as SAZ-1 zeolite and the relative energies of individual structures are also similar to SAZ-1 (Table 4.5). The shifted IPC-16 analogue has one more level of disorder than SAZ-1, as the channel structure after the layer shift allows the disorder of the S4R units also in the other crystallographic direction (Figure 4.7). All three types of disorder were investigated on 12 structures of shifted IPC-16 analogues (Table 3.1, Table 4.5). All shifted zeolite structures are significantly higher in energy than IPC-16, due to a very high strain in the structure imposed by S4R. None of the shifted IPC-16 analogue structure fulfils all LID criteria, which are otherwise satisfied by all other zeolites in SAZ-1P family (Table 4.5). The number of missed LID criteria correlates directly with the relative energy of the structure.

In summary, the structure of SAZ-1 zeolite was identified, together with IPC-15 and IPC-16 and other potential products of the ADOR strategy. As shown previously in the case of IPC-1P zeolite family, the zeolites with the same layer arrangement as the original material are the most stable. Furthermore, the SAZ-1 zeolite and its S4R containing analogues show a unique type of disorder; they are structurally very well defined but their crystal structure contains inherently statistical domains. They thus are the first confirmed zeolites with a statistical structure. Part of the reported results is included in Ref. [70], included in this thesis as Attachment D.

4.1.3 MCM-22P and MCM-56 layered zeolites

MCM-22P is a layered precursor of the zeolite MWW. The layered precursor is a primary product of the synthesis of MCM-22 zeolite, whereas 3D zeolite is only formed by the calcination of the MCM-22P layers. MCM-22P is a well ordered material with strong hydrogen bonding between the layers. Besides MCM-22P there are several known layered materials derived from MWW layers including MCM-56,[20] EMM-10P or ITQ-2. The zeolite MCM-56 is a strongly disordered material with an undefined layer stacking. MCM-56 is obtained by stopping the synthesis of MCM-49 zeolite

(zeolite with MWW topology) before the ideal 3D zeolite structure is formed. While the structure of individual MWW layers is known, the exact structure of neither MCM-22P nor MCM-56 has been solved. The aim of this project was to investigate the interaction of MWW layers and to identify the full 3D structure of experimentally known materials by simulating their pXRD patterns.

MCM-22P layers have a relatively low concentration of surface silanols (1.1 silanols/nm^2), which are 8.2 Å from each other. There are three possible interaction modes of the layers identified by the DFT calculations (at vdW-DF2 level): i) the "stack" structure with weakly interacting silanol groups just above each other (Figure 4.8a); ii) the "hydrogen-bonded" structure (HB, Figure 4.8b) with a strong linear hydrogen bond formed by a small lateral shift of layers; and iii) "submerged" structure (SM, Figure 4.8c) with layers shifted by half a UC and collapsed into cavities on the MWW surface. The layers in the SM have a maximized dispersion interaction due to smaller interlayer distance, but the hydrogen bonding between the layers is rather weak, because the hydrogen bonds form only between silanols and framework oxygens. The collapsed structure is distinctly different from structures formed by IPC-1P and SAZ-1P layers and is possible only due to the small concentration of surface silanols.

The structures of interacting layers were optimized both without and with an SDA, particularly hexamethyleneimine (one or two molecules per UC). This SDA was used experimentally to reversibly convert MCM-56 structure to MCM-22P; the MCM-56 is re-obtained by acidification of the solution and washing of the SDA from the MCM-22P.[85] The SM structure is the most stable structure without any SDA (Table 4.6). The presence of SDA enables the formation of an HB structure, which is the most preferred one for high SDA concentration. The change in relative stabilities, as well as changes in layer distances, suggests that the HB structure could be assigned to MCM-22P and SM to MCM-56 materials.

The powder diffraction patterns of all predicted structures were simulated to compare them with the experimentally known materials. The positions of the diffraction peaks of the HB structure perfectly match the MCM-22P data (Figure 4.9). The only significant difference is in the shape of some peaks around 10°, which show much finer structure than the experimental pattern. This discrepancy can be removed by the

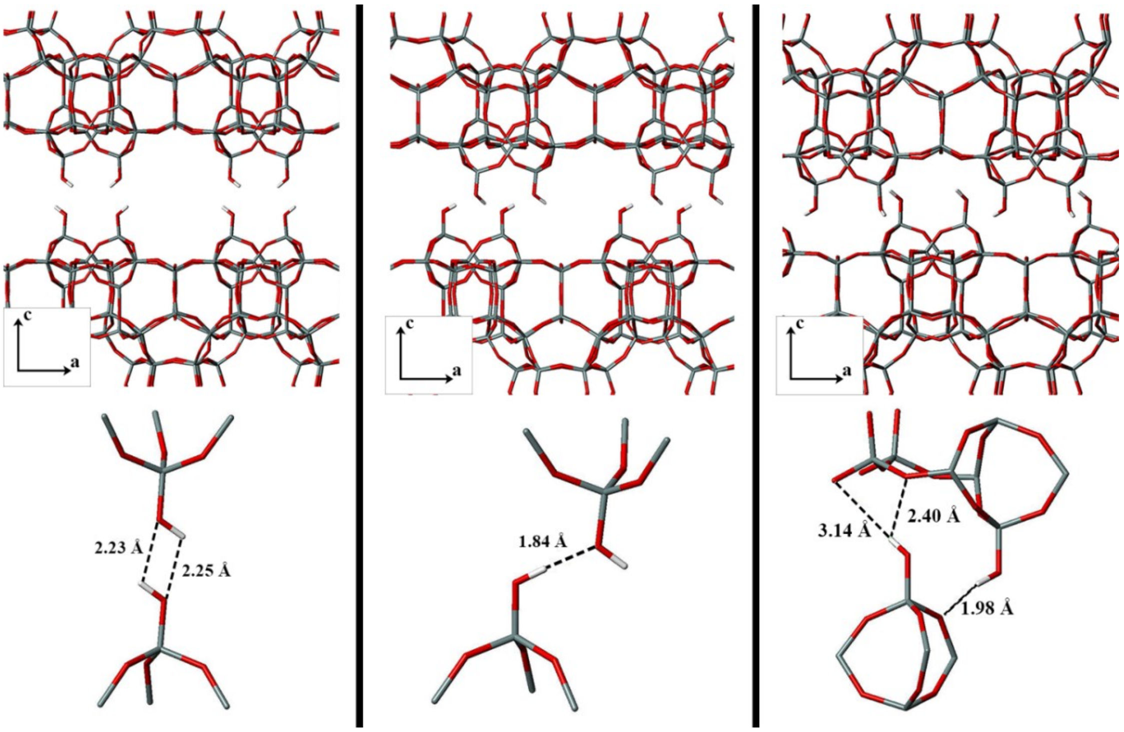

Figure 4.8 – Three modes of inter-layer interactions found at the vdW-DF2 level for MWW layers: stack (left), HB (middle) and SM (right) arrangements; SDA molecules are not shown. Colour scheme: O, Si and H in red, grey and white, respectively. Adapted from Ref.[86] with permission from the Royal Society of Chemistry.

Table 4.6 – Relative energies and layer distances of different arrangements of MCM-22P layers obtained at vdW-DF2 level

		HB	Stack	SM
no SDA	E_{rel}[a]	-	30.1	0
	d[b]	-	28	25
1 SDA	E_{rel}[a]	15	-	0
	d[b]	27	-	25
2 SDA	E_{rel}[a]	0	79	5
	d[b]	27	28	25
Exp.	c[c]	~27		~25
		MCM-22P		MCM-56

[a] Relative energies in kJ mol^{-1} per UC
[b] perpendicular distance between layers, in Å
[c] c vector length in Å, from Ref. [87]

introduction of the small disorder in the HB layer arrangement. The hydrogen bonds between layers can have six symmetrically (and energetically) equivalent directions. However, in the set of more than two interacting layers, combinations of the bond directions become inequivalent. A model of randomized crystals with 30 MWW layers and a random selection of the shift direction was constructed and used to simulate diffraction patterns, leading to an excellent agreement with the experiment (Figure 4.9b).

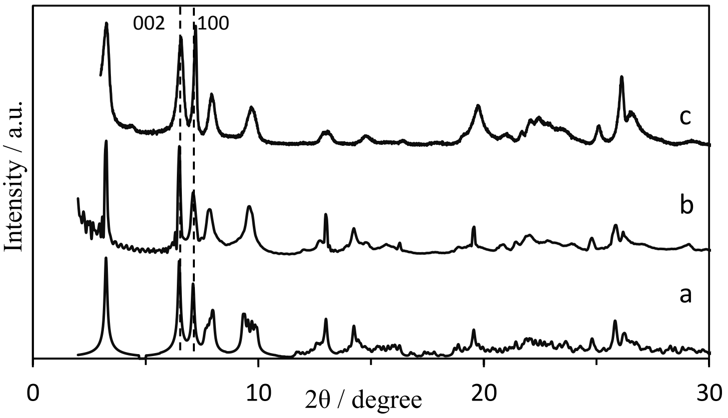

Figure 4.9 – Simulated XRD patterns for regularly (a) and randomly (b) arranged HB layers (randomness just within the six possible H-bond orientations) and the experimental MCM-22P XRD pattern (c). Reproduced from Ref. [86]with permission from the Royal Society of Chemistry.

The positions of the main peaks in SM and MCM-56 pXRD patterns are in good agreement, but the SM pattern lacks several important features, especially the broad band in region 7.5-10°. SM structure can be randomized by taking symmetry into account, similarly to HB, but the pXRD pattern does not improve (Figure 4.10a). However, there are other possible sources of disorder in the SM structure. Firstly, the hydrogen bonding between the SM interacting layers is very weak and there are many local minima produced by lateral shift of the layers. The layers can thus in principle slide on each other without a significant change in energy. This corresponds to the experimentally based hypothesis that the disorder in MCM-56 material originates from a complete lack of crystallographic order between the layers[87]. The stacking disorder was modelled by a random shift of the layers along four crystallographic directions (the shift cannot be completely random as the surface silanol groups must avoid each other). The resulting pattern produces a broad band of the same size as the experimental one (Figure 4.10b). Secondly, the shape of the broad band depends on the synthetic procedure material. MCM-56 is obtained by a premature stopping of the MCM-49 zeolite synthesis. The MCM-56 can thus contain domains of already condensed layers.[88] To model this structural disorder a part of the layers was connected directly forming thin blocks of MWW zeolite (by rolling dice for every interlayer space). The best agreement with the experiment was found for the structure with 70 % of the randomly shifted SM and 30 % of condensed layer. Combination of both interlayer shifts and partial condensation of the layers provides an excellent match with the experiment (Figure 4.10c).

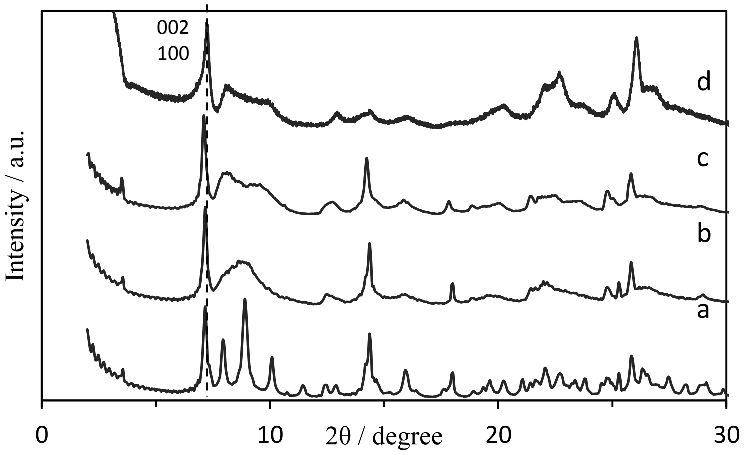

Figure 4.10 – XRD patterns of SM with regular shifts between layers (a); SM with random translation of adjacent layers (b) and crystal containing 70 % of SM (with random translation) and 30 % of MWW (c) compared with experimental patterns of MCM-56 (d). Reproduced from Ref.[86] with permission from the Royal Society of Chemistry.

In summary, three possible interaction modes of the MWW based layers were proposed based on the DFT calculations. The relative energies of the possible interaction modes strongly depend on the presence of SDA, which stabilizes a well--ordered H-bonded structure. This structure corresponds to the MCM-22P zeolite, which was confirmed by the simulated powder diffraction patterns. A disorder in MCM-22P structure should be taken into account to achieve a good agreement of simulated and experimental patterns. The most stable structure without SDA was a collapsed "submerged" structure which was identified as MCM-56 zeolite. This material contains a large degree of translational disorder between the neighbouring layers. Also, development of peaks at 8 and 10.1° 2θ, characteristic for MCM-56, is an indication of increased condensation of neighbouring layers in the MCM-56 material. Results reported herein show that the simulation of powder XRD patterns of finite-size crystals is a useful approach for identification of the structure of lamellar zeolites. The results were reported in Ref. [86] and are included in this thesis as Attachment E.

4.1.4 Hierarchical USY zeolite

Recently a hierarchical zeolite derived from zeolite USY (a high-silica form of FAU) was found to have strong basic catalytic properties which were completely lacking in its parent material.[89, 90] USY zeolite with Si/Al ratio as high as 385 was treated by a weak alkali metal hydroxide, after which it showed high activity in several condensation reactions commonly catalysed by Brønsted bases. Basicity is not common in high-silica zeolites and is found mainly in high-aluminium zeolites with large content of costly additives like Cs^+ or grafted organic molecules. However, despite the lack of aluminium (and thus also of traditional acido-basic sites), the high basicity of hierarchical USY indicates that a different type of active sites is responsible for the catalytic activity. Therefore, it was hypothesised that Na^+ cations are grafted on the hierarchical zeolite surface during the base treatment and their charge is compensated by the deprotonation of silanol groups on the surface. In this chapter, the possible structure of the hierarchical faujasite surface is proposed as well as the structure of Na^+ active sites present in Na-USY zeolite.

A novel periodic model of hierarchical FAU was constructed containing a set of six sites that can be present on the faujasite hierarchical surface. Two groups of sites were considered (see Chapter 3.2.1 for more details); i) sites simulating surface of standard FAU zeolite, particularly surface D6R, surface S6R, and cavity in the cage (denoted S_{D6R}, S_{S6R}, and S_{06R}, respectively) and ii) defects on the zeolite surface formed by removing of individual T-atoms from the zeolite wall (B_{-1T}) and one or two T-atoms from the exposed hierarchical surface (S_{-1T} and S_{-2T}, respectively). The grafting of Na^+ ions was modelled by exchange of silanol hydrogen with Na^+ on each of the surface sites, forming a silanolate group similarly to the charged SDA adsorption in the case of IPC-1P zeolite. The resulting structures (Figure 4.11) strongly depend on the local concentration of surface silanols. The Na^+ ions in the surface sites interact with the silanolate groups and one or two other silanol oxygens. On the other hand, in the case of single atom defect sites the Na^+ and silanolate do not interact directly; the Na^+ ion is rather coordinated by several OH groups which in turn coordinate the silanolate.

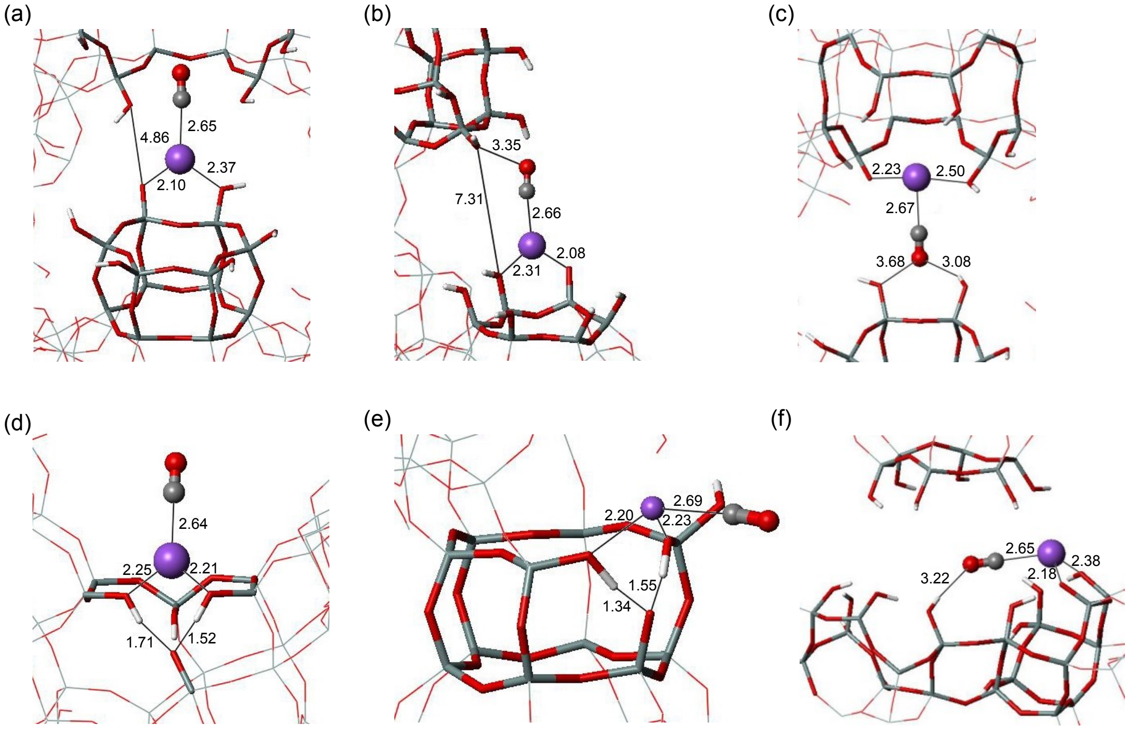

Figure 4.11 – CO adsorption complexes formed on (a) S_{D6R}, (b) S_{S6R}, (c) S_{06R}, (d) B_{-1T}, (e) S_{-1T}, and (f) S_{-2T} surface sites with grafted Na^+ ions in Na-hUSY. Si, O, H, and Na atoms are depicted in grey, red, white, and purple, respectively. All distances are indicated in Å. Reproduced with permission from Ref.[74] Copyright 2016 American Chemical Society.

The properties of all active sties were investigated by adsorption of CO molecular probe and by calculating of its stretching frequencies (Table 4.7). The IR spectra of the CO probe are commonly used to probe the acidobasic properties of the heterogeneous catalyst. The theoretical frequencies were calculated using the ω_{CO}/r_{CO} correlation of the CO frequencies calculated at the CCSD(T) level with the CO distances at the DFT level.[91] Both CO adsorption enthalpies and the vibrational frequencies are determined by two effects; the effect from the bottom and the effect from the top, which affect the experimental observations in opposing ways. The effect from bottom comes from the direct interaction of Na^+ ion with carbon in CO molecule. Typically, the high coordination of the cation leads to a weaker adsorption of the CO molecule, and thus a smaller blue-shift of the corresponding stretching frequencies. In contrast, the effect from top is caused by the interaction of CO (specifically the oxygen atom) with silanol groups in vicinity of the active sites, leading either to the red shift for CO interacting with silanol hydrogen or blue shift for interaction with oxygen.

Table 4.7 – Relative exchange energies, CO interaction energies, and CO stretching frequencies calculated at the PBE level for various surface sites grafted with Na^+ ions in Na-hUSY zeolites.

Site	Na-hUSY		
	$E_{ex}^{rel}(Na^+)$[a]	$E_{int}(CO)$[a]	$\nu_{\omega/r}(CO)$[b]
S_{06R}	27.4	-11.9	2167
S_{D6R}	61.5	-25.9	2176
S_{S6R}	76.2	-22.7	2178
B_{-1T}	0.0	-25.3	2180
S_{-1T}	11.0	-21.1	2174
S_{-2T}	11.7	-22.1	2162

[a] Energies in kJ mol^{-1}
[b] Frequencies in cm^{-1}

The CO interaction energies (at PBE level) range from range from −11.9 to −25.9 kJ mol^{-1} and the frequencies from 2160 to 2180 cm^{-1}. There is no correlation between the CO frequencies and interaction energies. Nevertheless, the frequencies were found to directly correlate with the strength of the effect from top on the CO molecule (Figure 4.11, Table 4.7). In structures like B_{-1T} the CO interacts only with the Na^+ ion leading to frequencies around at 2180 cm^{-1}. A weak interaction with distant silanols lowers the frequency to 2175 cm^{-1} (S_{D6R} site), whereas very strong interaction with silanols can shift the frequency even to 2162 cm^{-1} (S_{-2T} site). A very similar effect was also found for the K^+ exchanged hierarchical USY zeolite, in which the effect from top is even more pronounced due to the larger size of the cation (see Attachment F for the details). The range of obtained frequencies very well fits the observed experimental spectra proving the reliability of the model of hUSY surface. Nevertheless, the data show that CO molecule cannot serve as a probe of acidobasic properties of the hUSY material, because all information about the strength of the Na^+-CO interaction are hidden in the strong effect from top caused by interaction of CO with silanols in the vicinity of an active site.

In this project, we described for the first time the structure of alkali metal cationic sites grafted to USY zeolites. A novel model of hierarchical faujasite surface was developed containing a number of possible defects or surface sites for the Na^+ cations. We have simulated the adsorption of CO at six such possible active sites and calculated corresponding CO stretching frequencies. The results fit well the experimental spectra, confirming the reliability of the utilized model. The frequencies of CO are affected by the silanols on the hierarchical surface next to the active site. This “effect from top” is dominant over other contributions including strength of Na^+-CO interaction and thus hides any information about the acidobasic properties of active site. The whole study was published in a joint theoretical and experimental paper[74] and it is included in this work as Attachment F.

4.2 Microporous materials applications in catalysis

4.2.1 Na-hUSY catalytic activity in aldol condensation

The catalytic activity of Na^+ grafted hierarchical USY zeolite (see Chapter 4.1.4) was experimentally tested on several condensation reactions, for example the Knoevenagel condensation of benzaldehyde and malononitrile or the nitroaldol condensation of nitroethane with benzaldehyde.[90] The activity of the hierarchical material outperforms another tested basic zeolite Cs-X, in spite of very low aluminium content in the hierarchical USY (Si/Al ratio as high as 385). The activity was ascribed to the active sites formed by grafting of Na^+ ions on the hierarchical surface. Such sites were confirmed by a joint experimental and theoretical study to well explain the properties of the Na-hUSY zeolite (described in Chapter 4.1.4).[74] The herein reported study is a follow up project with an aim to thoroughly investigate the catalytic activity of Na-hUSY zeolite. Aldolization of acetone and furfural was selected as a model reaction (Scheme 4.1). This reaction is also a good model of deoxygenation reaction during the bio-oil upgrading processes.

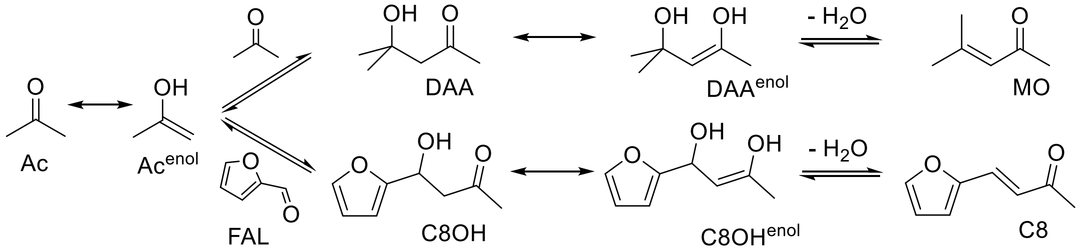

Scheme 4.1 – Overall reaction scheme of aldol condensation reactions occurring in acetone and furfural mixture. Top – self condensation of acetone, bottom – condensation of acetone and furfural.

The reaction of acetone and furfural was first investigated with computationally less demanding cluster models of individual active sites (Figure 3.2) at the

B3LYP/TZVP level of theory. The reaction profiles of aldol condensation of acetone and furfural strongly depend on the type of catalytic centre (Figure 4.12). The models of FAU surface sites provide a strong stabilization to the first transition state with barrier as low as 75 kJ mol^{-1}; almost half compared to both defect sites and standard Na^{+} faujasite. The barrier height of the first reaction step directly correlates with the accessibility of the silanolate group. Silanolate groups in the surface sites can interact directly with the enol form of acetone and have strong enough basic character to fully deprotonate it to enolate during the reaction (Scheme 4.2). The Brønsted basicity in the Na-hUSY material thus originates from the silanolate group, whereas the Na^{+} ions serve mainly as the activator of the catalyst. On the contrary the silanolate in defect sites is hidden in the surface and the sites thus exhibit only Lewis acid character.

The basicity of silanolate groups is the major contributor to the Na-hUSY activity. Nonetheless the Na^{+} ions also participate in the reaction as Lewis acid centres even in the FAU surface sites. Na^{+} ions are the main adsorption sites for the furfural molecule during the reaction and the reaction can thus be looked on as concerted Brønsted base – Lewis acid catalysed process (Scheme 4.2). The silanol groups surrounding the Na^{+} cation also join the reaction in what can be called the steric effect of the catalyst. In some sites the geometry of the hierarchical surface selectively stabilizes some transition states due to the fortuitous interaction with several silanol groups. This effect is strongest in the defect site S_{-2T}, which is the least active site in the first reaction step, whereas has similar activity to the most active site S_{S6R} in the dehydration step.

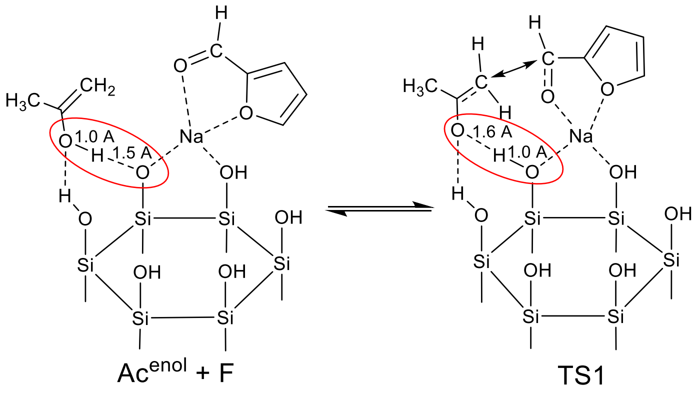

Scheme 4.2 – Basic properties of silanolate oxygen illustrated on the C-C coupling reaction step in aldol condensation of acetone and furfural on SS6R active site in Na-hUSY

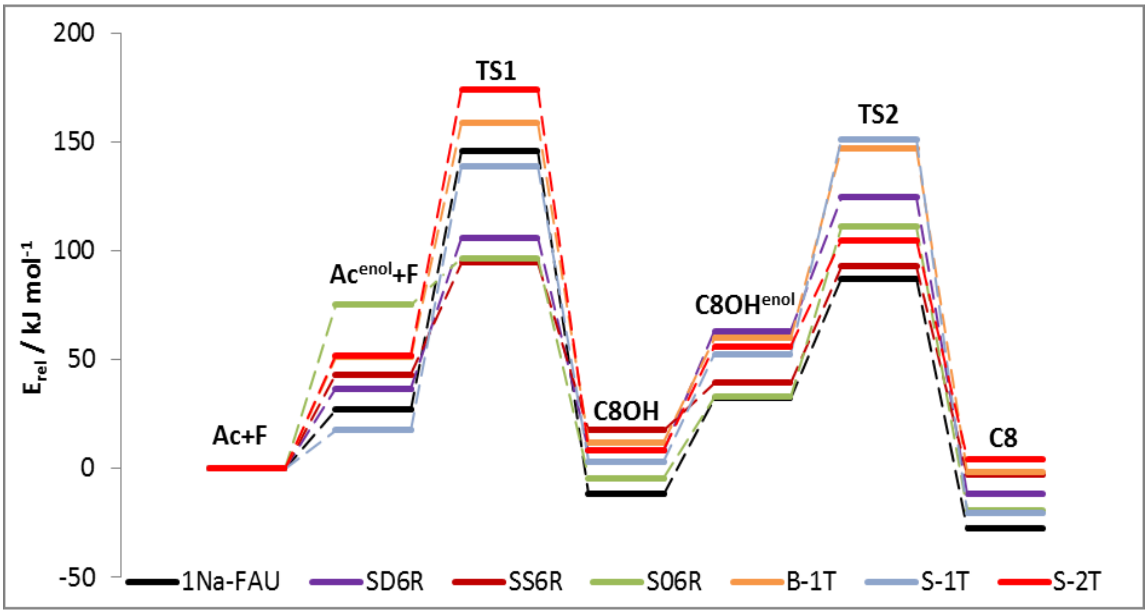

Figure 4.12 – Energy profile of acetone and furfural condensation catalysed by either Na-FAU or various Na-hUSY active sites. Energy of reactants interacting with the catalyst was chosen as relative zero in order to compare Na-FAU and Na-hUSY catalysts. All energies were obtained using cluster models and B3LYP/TZVP functional.

The aldol condensation of acetone and furfural catalysed by Na-hUSY was also tested by experimentally (in a collaborating group). The results showed that while Na-hUSY is active in the reaction it has a very low selectivity for it. The major observed process was a self-condensation of acetone, which ended after the C-C coupling step and the diacetone alcohol (Scheme 4.1) was the main obtained product. To explain this selectivity, the energies of minima on the reaction path self-condensation of acetone and condensation of acetone and furfural were compared theoretically using a periodic model of hierarchical surface and PBE+D3 functional. A new model of 2D FAU surface terminated by S6R groups (Na-S_{S6R}-hUSY) was constructed as a reliable model of the catalytically most active site (Figure 4.13). The reaction barriers of acetone self-condensation and acetone-furfural condensation reactions are almost identical (Table 4.8). Nevertheless, there is a large difference in the thermodynamics of both reactions. The first reaction step of acetone self-condensation on the Na-S_{S6R}-hUSY surface is 11 kJ mol^{-1} exothermic, whereas the acetone and furfural C-C coupling is 16 kJ mol^{-1} endothermic (Table 4.8). Contrarily, in the gas phase both reactions are 12 kJ mol^{-1} exothermic. This selective destabilization of the intermediate in the furfural condensation when adsorbed to S_{S6R} active site is thus responsible for the selectivity of

Na-hUSY material. Also the ultimate product of the acetone self-condensation is less stable than DAA on the hierarchical surface, which explains that the reaction stops only on the intermediate.

Table 4.8 – Reaction profiles of aldol condensations in acetone and furfural mixture catalysed by Na-S_{S6R}-hUSY catalyst. The energies of minima were calculated using PBE+D3 method and periodic modes and elementary step barriers were calculated using B3LYP/TZVP method and cluster model.

	structure	ΔE	$\Delta E^{\neq}_{cl}$		structure	ΔE	$\Delta E^{\neq}_{cl}$
Acetone+Acetone	Ac+Ac	-155		Acetone + Furfural	F+Ac	-188	
	$Ac+Ac^{enol}$	-128	56		$F+Ac^{enol}$	-160	51
	TS1	-72			TS1	-108	
	DAA	-166			C8OH	-172	
	DAA^{enol}	-111	38		$C8OH^{enol}$	-138	38
	TS2	-72			TS2	-100	
	$MO+H_2O$	-157			$C8+H_2O$	-205	

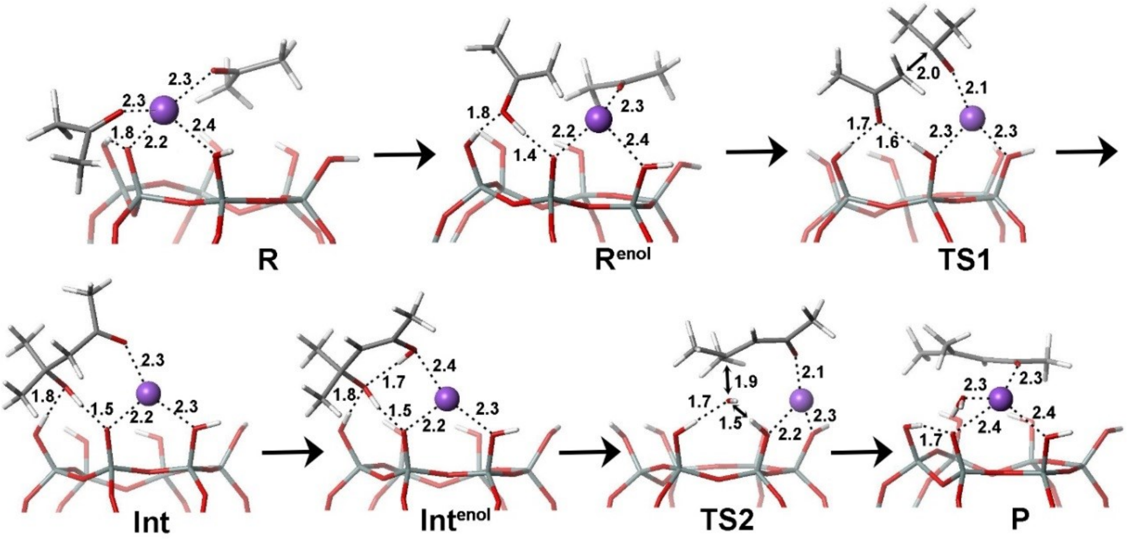

Figure 4.13 – Self-condensation of two acetone molecules catalysed by the S_{S6R} surface site in Na-hUSY. Structures obtained with S_{S6R} cluster model and B3LYP/TZVP method. Distances in Å. Si, O, C, H and Na atoms depicted in grey, red, dark grey, white and purple, respectively.

In conclusion, the catalytic activity of Na grafted hierarchical USY zeolite can be ascribed to the Brønsted basic silanolate groups that are formed on the hierarchical surface by deprotonation of surface silanols. The Na^+ ions themselves exhibit a Lewis acidic catalytic activity and support the catalysis by further activation of reactants. The large concentration of surface silanols was also shown to selectively promote some reaction steps by strong steric effects. The experimentally observed selectivity for the acetone self-condensation over the condensation of acetone and furfural originates from the destabilization of the acetone and furfural reaction intermediate compared to the reactants on the hierarchical surface, which makes the reaction thermodynamically unfavourable. The reported activity of Na-hUSY shows that the mesopores in the hierarchical materials do not necessarily just enhance zeolite diffusion properties, but can also contain new types of catalytically active site.

4.2.2 Photoreactivity in NO2-functionalized CAU-10

The metal-organic framework CAU-10-NO_2[92] was experimentally observed to exhibit unexpected photochemical reactivity[75]. An irradiation of this MOF by UV-light with wavelength of 365 nm (or just with sunlight) in an alcoholic solvent leads to a change in MOF colouring. The EPR measurements revealed the formation of stable radicals in the organic linker after the irradiation. The amount of generated radicals depends on the size of the solvent molecules with ethanol providing the highest activity, followed by methanol and propanol. DFT calculations were carried out to gain insight into the photochemical reactions inside CAU-10-NO_2 MOF and mainly to discern the nature of the formed stable radicals.

CAU-10-NO_2 MOF consists of rods of aluminium hydroxide interconnected via 5-nitroisophtalate linkers. The structure of MOF was obtained from the vdW-DF2 calculations based on the experimental UC size and the expected structure. The resulting structure corresponds well to the experimental characteristics. The structure of the MOF contains 1D pores formed of the nitrobenzene units with narrow openings lined by four nitro groups. The photochemical reduction of this structure was studied using methanol as the solvent. Methanol preferably interacts with organic linkers; a combination of electrostatic and dispersion interaction results in a structure where methanol is placed above the nitrobenzene unit (Figure 4.14). The methyl group interacts with the benzene ring via dispersion and the hydroxyl interacts with the NO_2 group.

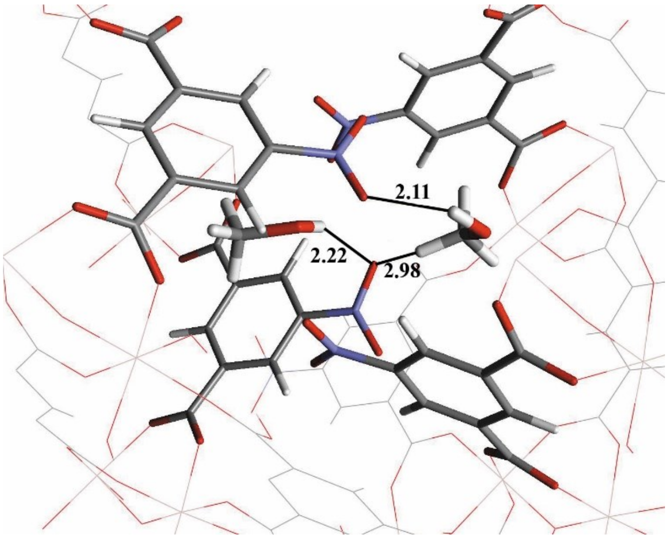

Figure 4.14 – Structure of two methanol molecules interacting with CAU-10-NO_2; the energetically lowest structure obtained at the vdW-DF2 level using periodic model. Distances in Å; C, H, O, and N atoms depicted in grey, white, red, and blue colour, respectively. Reproduced with permission from Ref.[75] Copyright 2015 American Chemical Society.

The calculations of electronically excited states were performed with a cluster model of 5-nitroisophtalate (charge compensated by Li^+ ions) and a single molecule of methanol at the CC2[93] level of theory. The Figure 4.15 summarizes the photochemical processes and all reaction energies. The vertical S1←S0 absorption due to a π*←n transition is characterized by an excitation energy of 352 kJ mol^{-1} (340 nm). The geometry optimization at the S1 excited state leads towards the conical intersection between S0 and S1 states. The S1 formation is accompanied by significant prolongation of one of the N-O bonds to1.64 Å (structure II in Figure 4.15). The N-O bond becomes even longer at the conical intersection. There are two paths exiting the conical intersection: i) the oxygen atom re-attaches to the nitrogen and the system returns to the electronic ground state structure, or ii) the oxygen atom attacks the methanol molecule and a nitroso group is formed on the benzene ring (Figure 4.15).

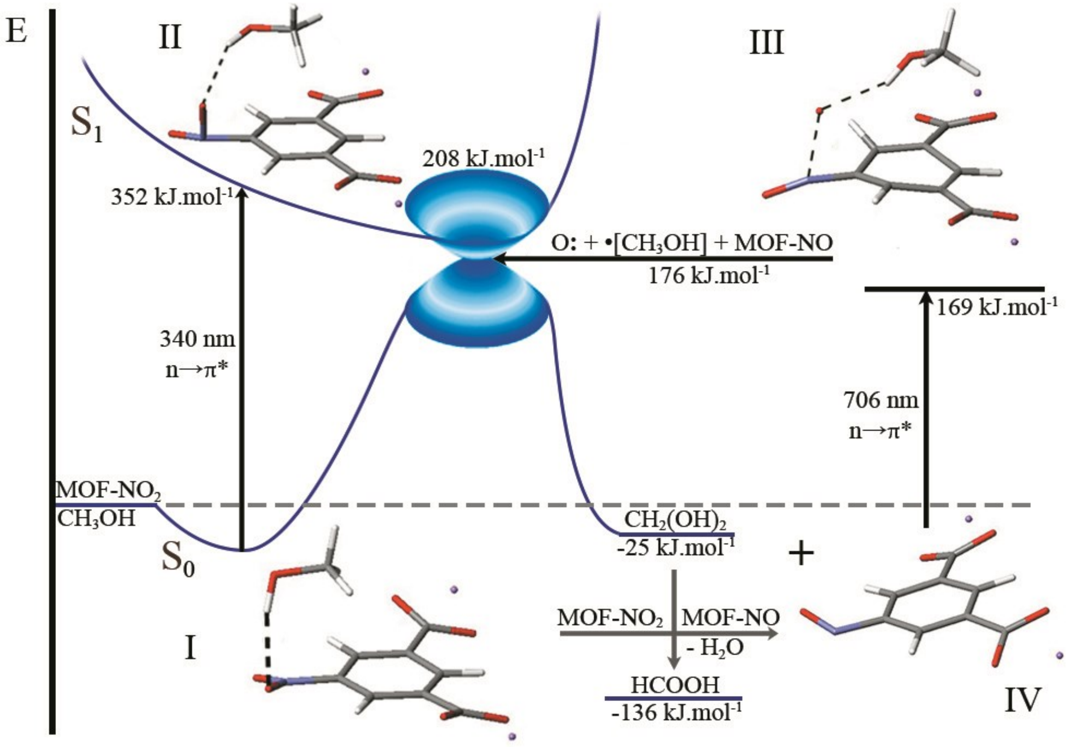

Figure 4.15 – Photochemical conversion of 5-notroisophatalte to 5-nitrosoisophtalate investigated at the CC2 level of theory. Relative energies with respect to non-interaction methanol and lithium 5-notroisophatalte molecules reported in kJ mol^{-1}. Conical intersection depicted as blue cone. Vertical excitation energies are also reported (in nm). C, H, O, and N atoms depicted in grey, white, red, and blue colour, respectively. Reproduced with permission from Ref.[75] Copyright 2015 American Chemical Society.

Calculated vertical excitation energies for 5-nitrosoisophtalate (706 nm) is in reasonable agreement with the experimental results of the irradiated CAU-10-NO_2, confirming the formation of nitroso group. The presence of the nitroso group also well explains the radical detection by the EPR spectroscopy. The methanol molecule attacked by the oxygen radical forms an unstable diol or peroxide, which readily decompose to formaldehyde (Scheme 4.3). Due to the large local concentration of nitro groups, formaldehyde or the unstable intermediates can be also attacked by another oxygen radical though, which results in the formic acid formation. Formic acid was also detected experimentally in the solvent after the MOF irradiation.

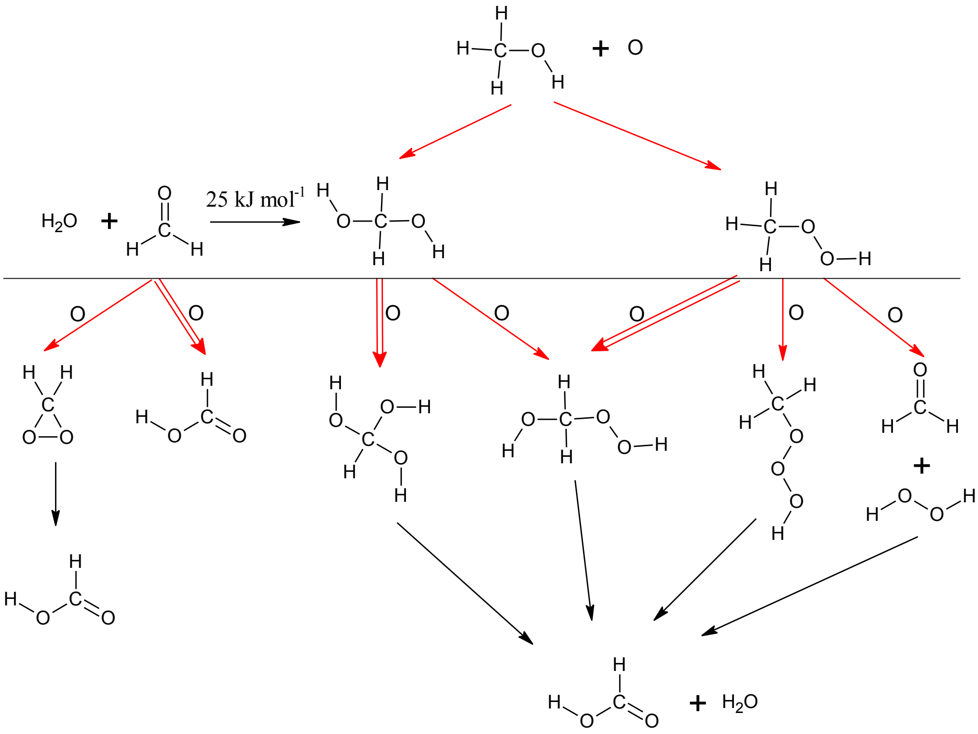

Scheme 4.3 – Reaction scheme showing the reaction of oxygen atom formed photochemically with methanol (upper part) and with the product of first oxidation reaction (lower part). Red and black arrows denote reaction photochemical and thermal reactions, respectively. All processes are exothermic at the B3LYP/6-311(2d,p) level of theory. Reproduced with permission from supplementary information of Ref.[75] Copyright 2015 American Chemical Society.

In this project, the CAU-10-NO_2 structure was confirmed theoretically and shown to contain 1D channels with surface formed by 5-nitroisophtalate linkers. In the presence of alcoholic solvent, the S_1 excited state of the linkers has a significantly prolonged NO bond and the conical intersection between S_1 and S_0 can also lead towards formation of nitroso group. The predicted excitation energies of both nitro- and nitroso-substituted linkers agree with the experiment. The presence of nitroso groups also well explains the experimentally observed EPR spectra. This project was published in a joint experimental and theoretical study[75] which is attached to this work as Attachment G.

4.2.3 Knoevenagel reaction catalysed by CuBTC

The metal organic framework CuBTC (also known as HKUST-1)[25] is one of the most studied MOFs thanks to its low price, high efficiency in adsorption, and high activity in catalysis. CuBTC contains Cu^{2+} ions interconnected via benzene-1,3,5-tricarboxylate linkers, which form a so called "paddlewheel" unit that consists of Cu^{2+} pairs coordinated via four carboxylic linkers. The paddlewheel has two coordinatively unsaturated sites (*cus*), which are very strong adsorption and Lewis acid catalytic sites. CuBTC was found to have a rather high catalytic activity in a Knoevenagel reaction,[94] which is quite puzzling, considering the fact that CuBTC contains only Lewis acid sites, whereas the Knoevenagel reaction is commonly catalysed by bases. In order to explain the experimentally observed activity, a mechanism for the Knoevenagel reaction of malononitrile and benzaldehyde catalysed by CuBTC was computationally investigated.

Part of this project was already included in my diploma thesis, where I reported the investigation of the Knoevenagel reaction using cluster model of the catalyst. Herein I present an expanded investigation of the reaction using periodic model of the CuBTC catalyst, which was found necessary to properly describe the CuBTC catalytic activity. This expanded project resulted in a publication in the ChemCatChem journal[95] and it is attached as Attachment H.

The Knoevenagel reaction mechanism was studied using a fully periodic structure of CuBTC at the vdW-DF2 level. The most common mechanism for the Knoevenagel reaction is based on the deprotonation of an active methylene compound by a basic catalyst. Due to the lack of basic catalytic sites an alternative mechanism was proposed; the reaction on the CuBTC catalyst comprises of two independent parts, i) an activation of the catalyst by the reactants, and ii) the condensation reaction (Figure 4.16). The malononitrile molecule adsorbs on two *cus* sites in the CuBTC simultaneously with a Cu-N distances of 2.4 Å (Figure 4.17). In the first part of the reaction, malononitrile is deprotonated and simultaneously a defect on one of the participating paddlewheel units is formed. The defect is created by the transfer of a proton from malononitrile onto the paddlewheel to form a -COOH group from one of the carboxylate ligands (Figure 4.17a). Proton is too far from the carboxylate group (5.9 Å) for the reaction to proceed in one step, but the proton transfer can be mediated by other molecules present in the pore (*e.g.* by benzaldehyde). A covalent bond is formed between malononitrile nitrogen and Cu atom on paddlewheel to compensate the charge on copper atom (Figure 4.17b). The energy of the defect with adsorbed reactants differs significantly in periodic and cluster model of the catalyst (comprised of two paddlewheel units connected via phenylene linker, Figure 4.18).

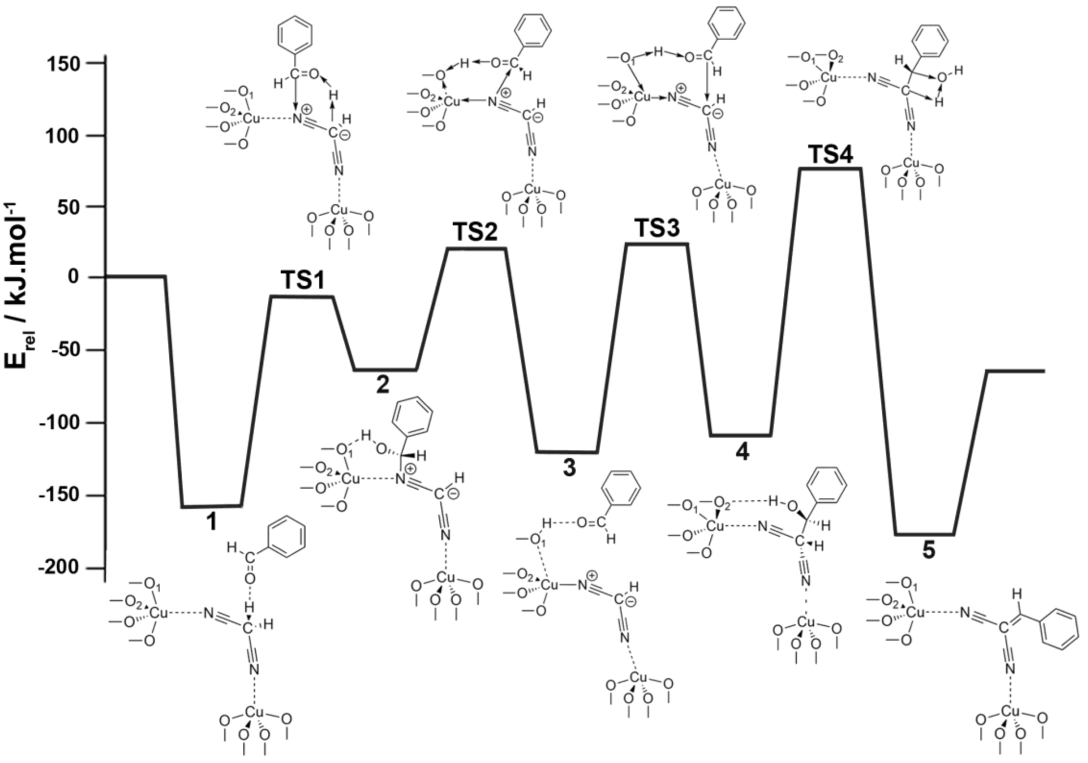

Figure 4.16 – Energetics and structures of minima and transition states on the reaction path of the Knoevenagel reaction catalysed by CuBTC. Reproduced with permission from Ref.[95] Copyright 2014 Wiley.

The second part of the reaction step comprises of the C-C bond formation between the malononitrile and benzaldehyde followed by the dehydration of intermediate and simultaneous healing of the defect. The Brønsted acid site in the defect is the strongest adsorption site for the benzaldehyde in CuBTC and also strongly activates benzaldehyde for the reaction. At the same time the deprotonated malononitrile is immobilized on the defect *cus* site, which acts as a strong Lewis acid. Both reactants are thus strongly activated for the C-C coupling step. The following dehydration step is

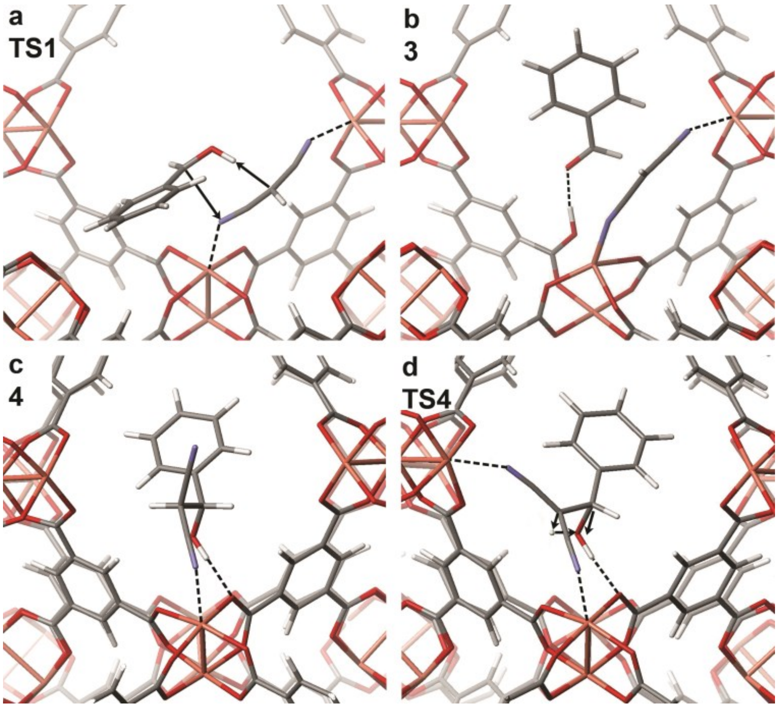

Figure 4.17 – a) **TS1**, transition state for the malononitrile deprotonation; b) **3**, deprotonated malononitrile and benzaldehyde bound to the defect; c) **4**, intermediate before a dehydration; d) **TS4**, the transition state for the final dehydration and double bond formation step. Structure numbering corresponds to Figure 4.16. C, O, N, H, and Cu depicted in grey, red, blue, white, and pink, respectively. Reproduced with permission from Ref.[95] Copyright 2014 Wiley.

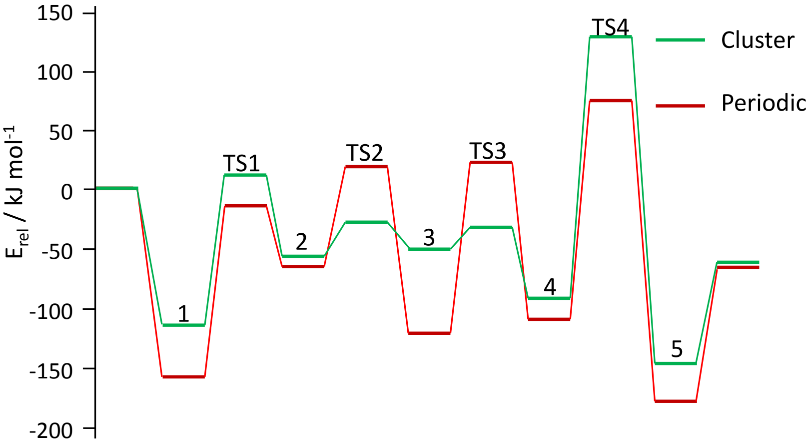

Figure 4.18 – Reaction profile of the Knoevenagel reaction catalysed by the CuBTC obtained with the cluster (green bars) and periodic (red bars) CuBTC models. All energies were obtained at vdW-DF2 level of theory. Reproduced with permission from supplementary information of Ref.[95] Copyright 2014 Wiley.

affected by a steric effect of the CuBTC material. The intermediate after the C-C bond formation does interact only with one *cus* site (Figure 4.17c), whereas the following dehydration transition state is affected by two *cus* sites (Figure 4.17d). However, in CuBTC this process can proceed with a decreased barrier on a different pair of Cu^{2+} ions than the first part of the reaction, which causes the discrepancy between the cluster and periodic model in the last step (Figure 4.18). The change in the interaction mode during the reaction is a very important property of MOFs with a high active-site concentration, as the readsorption of intermediates on a different site can affect the reaction mechanism.

In summary, critical features of the CuBTC catalytic activity in the Knoevenagel reaction were identified. The CuBTC acts as a Brønsted base and accept a proton from the malononitrile molecule, which is accompanied by formation of a defect in the paddlewheel unit. The thus-formed pair of a Lewis acid site (Cu^{2+}) and an adjacent Brønsted acid site (-COOH) compose the catalytic centre for the Knoevenagel reaction. The CuBTC is thus activated by the reactant molecules themselves. Another important aspect of the CuBTC activity is the simultaneous involvement of adjacent Cu^{2+} sites in the supercage that are ideally arranged for malononitrile interaction with two *cus* sites simultaneously. This steric effect leads to the decrease of reaction barriers and the full periodic model of CuBTC was found necessary to properly describe the CuBTC role in the Knoevenagel reaction.

5. Conclusions

The aim of this thesis was to provide an insight in the structure and experimentally observed properties of novel microporous materials, particularly hierarchical zeolites derived from zeolites UTL, SAZ-1, MWW, and FAU and metal organic frameworks CuBTC and CAU-10. The whole work was purely computational and was done with quantum chemical methods based on the density functional theory. However, all projects were done in a close collaboration with experimental groups and high emphasis was given to ensure the comparability of the computational models and experiment.

The thesis contained seven loosely connected topics that can be divided into two main groups; i) the investigation of structures of new microporous materials, particularly new zeolites, and ii) the investigation of reactivity and catalytic activity of microporous materials. Following conclusions can be drawn:

i. ***Structure of layered materials***

Structures of layered zeolites IPC-1P (derived from UTL framework), SAZ-1P (derived from SAZ-1), and MCM-22P (derived from MWW) were obtained using realistic models of periodically interacting layers. All materials share a common structural motif of layers connected via strong linear hydrogen bonds accompanied by a small lateral shift of the layers. The structure of layered zeolites is also strongly affected by concentration and arrangement of silanols on the zeolite surface. The low concentration of silanols in MWW zeolites allows for another structural motif – collapsed layers with non-interacting silanols from opposite layers. The stability of such arrangement is driven by dispersion interactions. This structure was found to correspond to the zeolite MCM-56. The large silanol concentration in IPC-1P and SAZ-1P zeolites enables several unique arrangements of the layers, produced by a shift of the layers by half a unit cell along in-plane crystallographic vectors. All these structures are stabilized by hydrogen bonding.

ii. ***Structure of new zeolites***

The layered zeolites can be reconnected to form standard 3D zeolites. IPC-1P and SAZ-1P, obtained by a removal of part of the parent zeolite structure, form previously unknown zeolites upon reconnection. This process of new zeolite synthesis through layered zeolites is called ADOR. The new zeolites can be created by either direct reconnection of the layers, or by adding silicon bridges in-between the layers. Thanks to the high concentration and arrangement of the silanols in SAZ-1P and IPC-1P, the silicon bridges are combined into single-four membered ring units and the interlayer expanded materials are also zeolites (full connectivity criteria). Furthermore, both IPC-1P and SAZ-1P can produce several new zeolites based on different layer arrangements. Therefore, two sets of new zeolite structures for both IPC-1P and SAZ-1P (directly reconnected and interlayer expanded) were predicted herein and used to resolve the experimental structures. The structures of six new zeolites IPC-2, IPC-4, IPC-9, IPC-10, IPC-15 and IPC-16 were thus identified.

iii. Effect of the SDA and pH

The ADOR process of new zeolites synthesis relies on a use of SDA molecules to organize the zeolite layers. Molecules like octylamine were experimentally found to significantly improve the quality of zeolite IPC-4, obtained by direct reconnection of IPC-1P layers. The theoretical investigation of the octylamine effect on the IPC-1P layers showed that it significantly stabilizes the arrangement leading to IPC-4. The effect of SDA is rather different when basic conditions and a charged SDA, *e.g.* choline cation, are used. Under high pH, the silanol groups deprotonate to silanolates and the IPC-1P surface becomes charged. The resulting electrostatic repulsion causes layers to shift, explaining the formation of new zeolites IPC-9 and IPC-10.

Deprotonation of surface silanols in high pH can also play significant role in catalytic properties of hierarchical materials. The silanolate groups on the mesopore surface in USY zeolite, obtained by exchange of silanol hydrogens by Na^+ ions, were shown to exhibit a strong basic catalytic activity in the aldol condensation of acetone and furfural. The silanolate groups act as strong Brønsted base catalytic centres for this reaction.

iv. *Disorder*

All studied lamellar zeolites contain certain level of disorder. The nature of the disorder was studied for the layered zeolites with MWW topology, MCM-22P and MCM-56. The structures of finite size crystallites of both zeolites were modeled and compared to experiment by simulation of powder diffraction patterns. MCM-22P has a rather well-defined structure, only a small disorder is observed, due to several symmetrically equivalent directions of interlayer hydrogen bonding. On the contrary, MCM-56 is a highly disordered material with layers collapsed into each other. The interaction between the layers is dominated by dispersion, resulting in a large degree of translational disorder. Furthermore MCM-56 was found to contain domains of 3D MWW zeolite.

Another studied statistical material was zeolite SAZ-1 and the derived S4R containing zeolites. The distribution of surface silanols on the SAZ-1P layers allows several equivalent arrangements of D4R (or S4R) in the zeolite, resulting in a set of possible SAZ-1 structures with very low energy differences. This leads to a statistical distribution of D4R in the SAZ-1 zeolite. The SAZ-1 zeolite is the first reported zeolite with such, completely statistical, structure.

v. *Defects*

The mesopore containing hierarchical zeolites can be viewed on as zeolites with a large concentration of surface defects. The USY mesopore surface was modelled by a set of several representative surface defects to explain the properties and catalytic activity of the Na^+ grafted USY zeolite. The structure of the surface defects was found to play a crucial role in the catalytic activity, caused by the silanolate groups. The single T-atom vacancies did not show any activity as the silanolate is blocked by the surface silanols in these sites. On the other hand, the open surface sites with a large concentration of surface silanols were found to be responsible for the strong catalytic activity of this material.

Metal organic frameworks are less chemically stable than zeolites and are thus often very prone to the formation of defects. This was well illustrated for CAU-10 MOF with nitro substituted linkers. Upon irradiation in the presence of an alcohol solvent, the CAU-10 MOF changes colour and permanent radicals are formed in its structure. This process was explained as follows; the nitro group in the linker was found to lose oxygen upon excitation, with alcohol serving as oxygen acceptor, forming nitroso groups on the linker.

The defects in MOF structure can be also formed dynamically during the catalytic process. CuBTC MOF was found to be able to serve as an acceptor for protons by forming a temporary defect in the structure. CuBTC, normally Lewis acidic catalyst, thus serves as a Brønsted base, strongly activating the reactants. The defect itself then acts as a catalytic centre for the rest of the reaction and it is healed in the last step of the reaction.

vi. Size of the computational model

The results for hierarchical zeolite USY and MOF CuBTC showed that the properties of microporous materials often originate from the large concentration of active sites that can simultaneously participate in the reaction. In the case of CuBTC catalysis of the Knoevenagel reaction, it is necessary to consider three neighbouring active sites to fully describe the optimal reaction path. The full periodic model was thus necessary to properly describe the material properties. Similarly, the two-layer models of layered zeolites, often used to describe a layer arrangement, were found to be inaccurate compared to the model of periodically interacting zeolite layers. Generally, the large role of the disorder and defects in the microporous materials reported above significantly increases demands on the size and quality of the models of microporous materials.

6. Bibliography

1. J. Rouquerol, D. Avnir, C. Fairbridge, D. Everett, J. Haynes, N. Pernicone, J. Ramsay, K. Sing and K. Unger, *Pure Appl. Chem.*, 1994, **66**, 1739-1758.
2. *Introduction to zeolite science and practice*, Elsevier, Amsterdam etc, 3rd ed. edn., 2007.
3. Z. Wang, J. Yu and R. Xu, *Chem. Soc. Rev.*, 2012, **41**, 1729-1741.
4. J. Yu and R. Xu, *Accounts of chemical research*, 2010, **43**, 1195-1204.
5. International zeolite associations, structure commission, http://www.iza-structure.org, 2017).
6. M. D. Foster and M. M. J. Tracy, A Database of Hypothetical Zeolite Structures: http://www.hypotheticalzeolites.net, 2016).
7. M. D. Foster, A. Simperler, R. G. Bell, O. D. Friedrichs, F. A. A. Paz and J. Klinowski, *Nat Mater*, 2004, **3**, 234-238.
8. R. Pophale, P. A. Cheeseman and M. W. Deem, *Phys. Chem. Chem. Phys.*, 2011, **13**, 12407-12412.
9. Y. Li, J. Yu and R. Xu, *Angew. Chem. Int. Ed.*, 2013, **52**, 1673-1677.
10. A. Corma, *J. Catal.*, 2003, **216**, 298-312.
11. A. Corma, V. Fornés, R. M. Martín-Aranda, H. García and J. Primo, *Applied Catalysis*, 1990, **59**, 237-248.
12. M. S. Holm, E. Taarning, K. Egeblad and C. H. Christensen, *Catal. Today*, 2011, **168**, 3-16.
13. W. J. Roth and J. Cejka, *Catal. Sci. Technol.*, 2011, **1**, 43-53.
14. W. J. Roth, P. Nachtigall, R. E. Morris and J. Cejka, *Chem. Rev.*, 2014, **114**, 4807-4837.
15. V. Valtchev, G. Majano, S. Mintova and J. Perez-Ramirez, *Chem. Soc. Rev.*, 2013, **42**, 263-290.
16. K. Na, M. Choi and R. Ryoo, *Microporous Mesoporous Mater.*, 2013, **166**, 3-19.
17. W. J. Roth, C. T. Kresge, J. C. Vartuli, M. E. Leonowicz, A. S. Fung and S. B. McCullen, *Stud. Surf. Sci. Catal.*, 1995, **94**, 301-308.
18. P. Wu, J. Ruan, L. Wang, L. Wu, Y. Wang, Y. Liu, W. Fan, M. He, O. Terasaki and T. Tatsumi, *J. Am. Chem. Soc.*, 2008, **130**, 8178-8187.
19. A. Corma, V. Fornés, J. Guil, S. Pergher, T. L. Maesen and J. Buglass, *Microporous Mesoporous Mater.*, 2000, **38**, 301-309.
20. *US Pat.,* 5,362,697, 1994.
21. A. Corma, U. Díaz, T. García, G. Sastre and A. Velty, *J. Am. Chem. Soc.*, 2010, **132**, 15011-15021.
22. W. J. Roth, J. Čejka, R. Millini, E. Montanari, B. Gil and M. Kubu, *Chem. Mater.*, 2015, **27**, 4620-4629.
23. G. Férey, *Chem. Soc. Rev.*, 2008, **37**, 191-214.
24. S. M. J. Rogge, A. Bavykina, J. Hajek, H. Garcia, A. I. Olivos-Suarez, A. Sepulveda-Escribano, A. Vimont, G. Clet, P. Bazin, F. Kapteijn, M. Daturi, E. V. Ramos-Fernandez, F. X. Llabres i Xamena, V. Van Speybroeck and J. Gascon, *Chem. Soc. Rev.*, 2017, **46**, 3134-3184.
25. S. S. Chui, *Science*, 1999, **283**, 1148-1150.

26. G. Férey, C. Serre, C. Mellot-Draznieks, F. Millange, S. Surblé, J. Dutour and I. Margiolaki, *Angewandte Chemie*, 2004, **116**, 6456-6461.
27. G. Férey, C. Mellot-Draznieks, C. Serre, F. Millange, J. Dutour, S. Surblé and I. Margiolaki, *Science*, 2005, **309**, 2040-2042.
28. J. Jiang and O. M. Yaghi, *Chem. Rev.*, 2015, **115**, 6966-6997.
29. L. Zhu, X.-Q. Liu, H.-L. Jiang and L.-B. Sun, *Chem. Rev.*, 2017, DOI: 10.1021/acs.chemrev.7b00091.
30. F. G. Cirujano, A. Leyva-Pérez, A. Corma and F. X. Llabrés i Xamena, *ChemCatChem*, 2013, **5**, 538-549.
31. J. Canivet, M. Vandichel and D. Farrusseng, *Dalton Transactions*, 2016, **45**, 4090-4099.
32. P. Silva, S. M. F. Vilela, J. P. C. Tome and F. A. Almeida Paz, *Chem. Soc. Rev.*, 2015, **44**, 6774-6803.
33. C. Cramer, *Essentials of computational chemistry : theories and models*, J. Wiley, West Sussex England; New York, 1st ed. edn., 2002.
34. W. Koch and M. C. Holthausen, *A chemist's guide to density functional theory*, John Wiley & Sons, 2015.
35. A. D. Becke, *The Journal of Chemical Physics*, 1993, **98**, 5648-5652.
36. C. Lee, W. Yang and R. G. Parr, *Phys. Rev. B*, 1988, **37**, 785-789.
37. J. P. Perdew and W. Yue, *Phys. Rev. B*, 1986, **33**, 8800-8802.
38. J. P. Perdew, K. Burke and M. Ernzerhof, *Phys. Rev. Lett.*, 1996, **77**, 3865-3868.
39. J. P. Perdew, J. A. Chevary, S. H. Vosko, K. A. Jackson, M. R. Pederson, D. J. Singh and C. Fiolhais, *Phys. Rev. B*, 1992, **46**, 6671-6687.
40. Y. Zhao and D. G. Truhlar, *Theoretical Chemistry Accounts*, 2008, **120**, 215-241.
41. S. Grimme, *J. Comput. Chem.*, 2004, **25**, 1463-1473.
42. S. Grimme, *J. Comput. Chem.*, 2006, **27**, 1787-1799.
43. S. Grimme, J. Antony, S. Ehrlich and H. Krieg, *The Journal of Chemical Physics*, 2010, **132**, 154104.
44. M. Rubes, P. Soldán, P. Nachtigall and O. Bludsky, *The Open Chemical Physics Journal*, 2008, **1**, 1-11.
45. M. Dion, H. Rydberg, E. Schröder, D. C. Langreth and B. I. Lundqvist, *Phys. Rev. Lett.*, 2004, **92**, 246401.
46. Y. Zhang and W. Yang, *Phys. Rev. Lett.*, 1998, **80**, 890-890.
47. O. A. Vydrov and T. Van Voorhis, *The Journal of chemical physics*, 2010, **133**, 244103.
48. K. Lee, É. D. Murray, L. Kong, B. I. Lundqvist and D. C. Langreth, *Phys. Rev. B*, 2010, **82**, 081101.
49. E. D. Murray, K. Lee and D. C. Langreth, *Journal of Chemical Theory and Computation*, 2009, **5**, 2754-2762.
50. G. Kresse, *Phys. Rev. B*, 1996, **54**, 11169-11186.
51. G. Kresse and J. Furthmüller, *Comput. Mater. Sci.*, 1996, **6**, 15-50.
52. G. Kresse and J. Hafner, *Phys. Rev. B*, 1993, **47**, 558-561.
53. G. Kresse and J. Hafner, *Phys. Rev. B*, 1994, **49**, 14251-14269.
54. G. W. T. M. J. Frisch, H. B. Schlegel, G. E. Scuseria, M. A. Robb, J. R. Cheeseman, G. Scalmani, V. Barone, B. Mennucci, G. A. Petersson, H. Nakatsuji, M. Caricato, X. Li, H. P. Hratchian, A. F. Izmaylov, J. Bloino, G. Zheng, J. L. Sonnenberg, M. Hada, M. Ehara, K. Toyota, R. Fukuda, J.

Hasegawa, M. Ishida, T. Nakajima, Y. Honda, O. Kitao, H. Nakai, T. Vreven, J. A. Montgomery Jr, J. E. Peralta, F. Ogliaro, M. Bearpark, J. J. Heyd, E. Brothers, K. N. Kudin, V. N. Staroverov, R. Kobayashi, J. Normand, K. Raghavachari, A. Rendell, J. C. Burant, S. S. Iyengar, J. Tomasi, M. Cossi, N. Rega, J. M. Millam, M. Klene, J. E. Knox, J. B. Cross, V. Bakken, C. Adamo, J. Jaramillo, R. Gomperts, R. E. Stratmann, O. Yazyev, A. J. Austin, R. Cammi, C. Pomelli, J. W. Ochterski, R. L. Martin, K. Morokuma, V. G. Zakrzewski, G. A. Voth, P. Salvador, J. J. Dannenberg, S. Dapprich, A. D. Daniels, Ö. Farkas, J. B. Foresman, J. V. Ortiz, J. Cioslowski and D. J. Fox, 2009.

55. A. Schafer, C. Huber and R. Ahlrichs, *J. Chem. Phys.*, 1994, **100**, 5829-5835.
56. J. D. Gale, *Journal of the Chemical Society, Faraday Transactions*, 1997, **93**, 629-637.
57. J. D. Gale and A. L. Rohl, *Molecular Simulation*, 2003, **29**, 291-341.
58. M. Sanders, M. Leslie and C. Catlow, *J. Chem. Soc., Chem. Commun.*, 1984, 1271-1273.
59. Mercury 3.1, Cambridge Crystallographic Data Centre., http://www.ccdc.cam.ac.uk/mercury/).
60. J. Boshoff, UDskip algorithm to calculate theoretical powder X-ray diffraction patterns of ultra-small zeolite crystals, www.che.udel.edu/research_groups/nanomodeling/resources.html.).
61. O. Bludský, M. Silhan, P. Nachtigall, T. Bucko, L. Benco and J. Hafner, *The journal of physical chemistry. B*, 2005, **109**, 9631-9638.
62. C. Peng and H. Bernhard Schlegel, *Israel Journal of Chemistry*, 1993, **33**, 449-454.
63. J. Kästner and P. Sherwood, *The Journal of chemical physics*, 2008, **128**, 014106.
64. D. Sheppard, P. Xiao, W. Chemelewski, D. D. Johnson and G. Henkelman, *The Journal of chemical physics*, 2012, **136**, 074103.
65. G. Henkelman, Vasp TST Tools, http://theory.cm.u-texas.edu/vrsttools/).
66. J.-L. Paillaud, B. Harbuzaru, J. Patarin and N. Bats, *Science*, 2004, **304**, 990-992.
67. L. Grajciar, O. Bludský, W. J. Roth and P. Nachtigall, *Catal. Today*, 2013, **204**, 15-21.
68. W. J. Roth, P. Nachtigall, R. E. Morris, P. S. Wheatley, V. R. Seymour, S. E. Ashbrook, P. Chlubna, L. Grajciar, M. Polozij, A. Zukal, O. Shvets and J. Cejka, *Nat. Chem.*, 2013, **5**, 628-633.
69. M. Mazur, P. S. Wheatley, M. Navarro, W. J. Roth, M. Položij, A. Mayoral, P. Eliášová, P. Nachtigall, J. Čejka and R. E. Morris, *Nat. Chem.*, 2016, **8**, 58-62.
70. D. S. Firth, S. A. Morris, P. S. Wheatley, S. E. Russell, A. M. Z. Slawin, D. M. Dawson, A. Mayoral, M. Opanasenko, M. Položij, J. Čejka, P. Nachtigall and R. E. Morris, *Chem. Mater.*, 2017, DOI: 10.1021/acs.chemmater.7b01181.
71. J. H. Kang, D. Xie, S. I. Zones, S. Smeets, L. B. McCusker and M. E. Davis, *Chem. Mater.*, 2016, **28**, 6250-6259.
72. M. A. Camblor, A. Corma, M.-J. Díaz-Cabañas and C. Baerlocher, *J. Phys. Chem. B*, 1998, **102**, 44-51.
73. J. L. Schlenker and B. K. Peterson, *J. Appl. Crystallogr.*, 1996, **29**, 178-185.
74. T. C. Keller, M. Položij, B. Puértolas, H. V. Thang, P. Nachtigall and J. Pérez-Ramírez, *J. Phys. Chem. C*, 2016, **120**, 4954-4960.

75. H. Reinsch, F. M. Hinterholzinger, P. Jäker, F. Hesse, B. Reimer, T. Bein, M. Položij, D. Nachtigallová, P. Nachtigall and N. Stock, *J. Phys. Chem. C*, 2015, **119**, 26401-26408.
76. W. J. Roth, O. V. Shvets, M. Shamzhy, P. Chlubna, M. Kubu, P. Nachtigall and J. Cejka, *J. Am. Chem. Soc.*, 2011, **133**, 6130-6133.
77. S. A. Morris, P. S. Wheatley, M. Polozij, P. Nachtigall, P. Eliasova, J. Cejka, T. C. Lucas, J. A. Hriljac, A. B. Pinar and R. E. Morris, *Dalton Transactions*, 2016, **45**, 14124-14130.
78. E. Verheyen, L. Joos, K. Van Havenbergh, E. Breynaert, N. Kasian, E. Gobechiya, K. Houthoofd, C. Martineau, M. Hinterstein, F. Taulelle, V. Van Speybroeck, M. Waroquier, S. Bals, G. Van Tendeloo, C. E. A. Kirschhock and J. A. Martens, *Nat Mater*, 2012, **11**, 1059-1064.
79. M. Trachta, P. Nachtigall and O. Bludský, *Catal. Today*, 2014, **243**, 32-38.
80. M. Trachta, O. Bludský, J. Čejka, R. E. Morris and P. Nachtigall, *ChemPhysChem*, 2014, **15**, 2972-2976.
81. V. Kasneryk, M. Shamzhy, M. Opanasenko, P. S. Wheatley, S. A. Morris, S. E. Russell, A. Mayoral, M. Trachta, J. Čejka and R. E. Morris, *Angew. Chem. Int. Ed.*, 2017, **56**, 4324-4327.
82. B. W. Boal, M. W. Deem, D. Xie, J. H. Kang, M. E. Davis and S. I. Zones, *Chem. Mater.*, 2016, **28**, 2158-2164.
83. Z.-H. Gao, F.-J. Chen, L. Xu, L. Sun, Y. Xu and H.-B. Du, *Chemistry – A European Journal*, 2016, **22**, 14367-14372.
84. M. Yoshikawa, P. Wagner, M. Lovallo, K. Tsuji, T. Takewaki, C.-Y. Chen, L. W. Beck, C. Jones, M. Tsapatsis and S. I. Zones, *J. Phys. Chem. B*, 1998, **102**, 7139-7147.
85. Y. Wang, Y. Liu, L. Wang, H. Wu, X. Li, M. He and P. Wu, *J. Phys. Chem. C*, 2009, **113**, 18753-18760.
86. M. Polozij, H. V. Thang, M. Rubes, P. Eliasova, J. Cejka and P. Nachtigall, *Dalton Transactions*, 2014, **43**, 10443-10450.
87. W. J. Roth, D. L. Dorset and G. J. Kennedy, *Microporous Mesoporous Mater.*, 2011, **142**, 168-177.
88. G. G. Juttu and R. F. Lobo, *Microporous Mesoporous Mater.*, 2000, **40**, 9-23.
89. D. Verboekend, T. C. Keller, S. Mitchell and J. Pérez-Ramírez, *Adv. Funct. Mater.*, 2013, **23**, 1923-1934.
90. T. C. Keller, S. Isabettini, D. Verboekend, E. G. Rodrigues and J. Perez-Ramirez, *Chemical Science*, 2014, **5**, 677-684.
91. D. Nachtigallová, O. Bludský, C. O. Areán, R. Bulánek and P. Nachtigall, *Phys. Chem. Chem. Phys.*, 2006, **8**, 4849-4852.
92. H. Reinsch, M. A. van der Veen, B. Gil, B. Marszalek, T. Verbiest, D. de Vos and N. Stock, *Chem. Mater.*, 2013, **25**, 17-26.
93. O. Christiansen, H. Koch and P. Jørgensen, *Chemical Physics Letters*, 1995, **243**, 409-418.
94. M. Opanasenko, A. Dhakshinamoorthy, M. Shamzhy, P. Nachtigall, M. Horáček, H. Garcia and J. Čejka, *Catal. Sci. Technol.*, 2013, **3**, 500-507.
95. M. Položij, M. Rubeš, J. Čejka and P. Nachtigall, *ChemCatChem*, 2014, **6**, 2821-2824.

7. List of Attachments

The thesis is based on eight articles, attached as Attachments A-H. Attachment I is a Declaration of authorship of the papers included in the thesis.

Attachment A:

Reprinted with permission from Macmillan Publishers Ltd: Nature Chemistry: "Roth W.J.; Nachtigall P.; Morris R.E.; Wheatley P.S.; Seymour V.; Ashbrook S.E.; Chlubná P.; Grajciar L.; **Položij M.**; Zukal A.; Shvets O. and Čejka J.: A family of complex zeolites with controlled pore size prepared through a 'top down' method. *Nature Chemistry* 5 (**2013**) 628–633". Copyright 2013.

To download this article and to access online supplementary information, please use: https://www.nature.com/nchem/journal/v5/n7/full/nchem.1662.html

Attachment B:

Reprinted from "Morris, S.A.; Wheatley, P.S.; **Položij, M.;** Nachtigall, P.; Eliášová, P.; Čejka, J.; Lucas, T.C.; Hriljac, J.A.; Pinar, A.B.; Morris, R.E.: Combined PDF and Rietveld studies of ADORable zeolites and the disordered intermediate IPC-1P. Dalton Trans. 45, (2016) 14124-14130." with permission from the Royal Society of Chemistry.

To download this article and to access online supplementary information, please use: http://pubs.rsc.org/en/Content/ArticleLanding/2016/DT/C6DT02612E#!divAbstract

Attachment C:

Reprinted with permission from Macmillan Publishers Ltd: Nature Chemistry: "Mazur, M; Wheatley, P.S.; Navarro, M.; Roth, W.J.; **Položij, M.;** Mayoral, A.; Eliášová, P.; Nachtigall, P.; Čejka, J.; Morris, R.E.: Synthesis of 'unfeasible' zeolites. *Nature Chemistry* 8 (**2016**) 58–62." Copyright 2016.

To download this article and to access online supplementary information, please use: https://www.nature.com/nchem/journal/v5/n7/full/nchem.1662.html

Attachment D:

Reprinted with permission from: "Firth, D.S.; Morris, S.A.; Wheatley, P.S.; Russell, S.E.; Slawin, A.M.Z.; Dawson, D.M.; Mayoral, A.; Opanasenko, M.; **Položij, M.;** Cejka, J; Nachtigall, P; Morris, R.E.: Assembly-diassembly-organisation-reassembly synthesis of zeolites based on cfi-type layers. *Chem. Mater.* (**2017**) doi: 10.1021/acs.chemmater.7b01181." Copyright (2017) American Chemical Society.

To download this article and to access online supplementary information, please use: http://pubs.acs.org/doi/abs/10.1021/acs.chemmater.7b01181

Attachment E:

Reprinted from "**Položij, M.;** Ho, V. T.; Rubeš, M.; Eliášová, P.; Čejka, J.; Nachtigall, P.: Theoretical investigation of layered zeolites with MWW topology: MCM-22P vs. MCM-56. *Dalton Transactions* 43 (**2014**) 10443-10450." with permission from the Royal Society of Chemistry.

To download this article, please use:
http://pubs.rsc.org/en/Content/ArticleLanding/2014/DT/C4DT00414K#!divAbstract

Attachment F:

Reprinted with permission from: "Keller, T.C.; **Položij, M.;** Puértolas, B.; Thang, H.V.; Nachtigall, P.; Pérez-Ramírez, J.: Understanding the Structure of Cationic Sites in Alkali Metal-Grafted USY Zeolites. *J. Phys. Chem. C* 120 (**2016**) 4954–4960." Copyright (2016) American Chemical Society.

To download this article and to access online supplementary information, please use: http://pubs.acs.org/doi/abs/10.1021/acs.jpcc.5b12413

Attachment G:

Reprinted with permission from: "Reinsch, H.; Hinterholzinger, F.M.; Jäker, P.; Hesse, F.; Reimer, B.; Bein, T.; **Položij, M.;** Nachigallová, D.; Nachtigall, P.; Stock, N.: Unexpected Photoreactivity in a NO_2-Functionalized Aluminum-MOF. *J. Phys. Chem. C* 119 (**2015**) 26401–26408." Copyright (2016) American Chemical Society.

To download this article and to access online supplementary information, please use: http://pubs.acs.org/doi/abs/10.1021/acs.jpcc.5b03138

Attachment H:

Reprinted with permission from: "**Položij, M.;** Rubeš, M.; Čejka, J.; Nachtigall, P.: Catalysis by Dynamically Formed Defects in a Metal–Organic Framework Structure: Knoevenagel Reaction Catalyzed by Copper Benzene-1,3,5-tricarboxylate. *ChemCatChem* 6 (**2014**) 2821-2824." Copyright 2014 Wiley.

To download this article and to access online supplementary information, please use: http://onlinelibrary.wiley.com/doi/10.1002/cctc.201402411/full

Attachment I:

Declaration of authorship specifying author's contributions on all papers included in the thesis.

Attachments: